Simulating the dynamics of deuterium and impurity puffing in a tokamak plasma towards the formation of an X-point radiator

van Tongeren, Jasper A.J.

Award date:
2023

EINDHOVEN UNIVERSITY OF TECHNOLOGY

Department of Applied Physics and Science Education

Simulating the dynamics of deuterium and impurity puffing in a tokamak plasma towards the formation of an X-point radiator

by

J.A.J. van Tongeren

MSC THESIS

Assessment committee	
Member 1 (chair):	prof. dr. ir. G.T.A. Huijsmans
Member 2:	prof. dr. R.J.E. Jaspers
Member 3:	dr. ir. M.R.A. Abdelmalik
Advisory member 1:	MSc S.Q. Korving
Advisory member 2:	dr. M. Hoelzl

Graduation	
Program:	Science and Technology of Nuclear Fusion
Capacity group:	Science and Technology of Nuclear Fusion
Supervisor:	prof. dr. ir. G.T.A. Huijsmans
Date of defense:	October 12, 2023
Student ID:	1016323
Study load (ECTS):	60

Abstract

The high confinement mode, called H-mode, which is the foreseen plasma configuration for high performance operation of the ITER tokamak, exhibits strong pressure gradients and current densities. These give rise to peeling and ballooning instablities, which together are suspected to result in edge localised modes, or ELMs. These ELMs cause large transient heat loads to the wall structures, reducing their lifetime in an unacceptable way. For DEMO, ELMs are expected to be intolerable all together. This means an effective power exhaust strategy is required, which radiates most of the heat away before the plasma reaches the wall.

One option for this is the X-point radiator, the XPR. Here, the region above the X-point of the divertor plasma undergoes a thermal collapse into the eV range, locally emitting radiation from impurities. Experiments on ASDEX Upgrade (AUG) show over 90% of the total heating power being radiated away in this fashion. Depending on the scenario, the XPR can offer a relatively well confined plasma regime without ELMs.

In this work the non-linear MHD code JOREK, with kinetic particle extensions, is used to study the XPR physics. The model used is a hybrid model built on reduced MHD with a single temperature assumption, as well as kinetic neutral deuterium particles and kinetic nitrogen impurities, which are treated with a particle in cell (PiC) approach. Just like in the experiments in AUG the deuterium and nitrogen are puffed from the divertor region.

An axissymmetric approach allows us to treat the case in just the poloidal cross section, allowing the investigation of detachment-like dynamics where the divertor targets exhibit a drop in temperature. It also allows us to investigate the convective transport of the nitrogen impurities.

As predicted from an analytical model exploring the possibility of an XPR, the plasma parameters in the X-point region and the outboard midplane reach a state that allows for an XPR to form. This XPR access condition, combined with the presence of nitrogen impurities, show a region approximately 4 cm above the X-point, where an XPR could form. The simulations did indeed develop a strongly localised radiator at this position. This result constitutes an important first step towards validation of JOREK models for interpretative and predictive XPR studies. Simulations over longer time scales, with stronger parameter variations, a fully self-consistent treatment of the electron density in the radiation calculation (which was simplified here), and eventually a full 3D treatment are logical next steps beyond this thesis.

Acknowledgements

I want to thank all my supervisors for helping me through this project. Matthias Hoelzl, who helped me from Germany, and always had useful insights. Guido Huijsmans, who always knew where to look in the code when I couldn't find something. Jan van Dijk, for his very useful insights as a non-fusion researcher. And Sven Korving, who helped me with the basics in the beginning, and was always quick to respond to my questions.

Contents

1 Introduction

Nuclear fusion is a way of harvesting clean energy that is currently being developed. This method of energy production mimics what is observed in stars. In the core of our sun, which is a hot plasma, hydrogen atoms fuse to form helium atoms [1]. However, it was found by Francis Aston that the mass of four hydrogen atoms was slightly larger than that of one helium atom. This difference in mass is 'lost' in the fusion process, and is released as energy, in accordance with Einstein's equation $E = mc^2$ [2]. For the production of energy on earth using nuclear fusion, a slightly different reaction is used, namely the fusion of deuterium (D) and tritium (T). These hydrogen isotopes fuse to form a helium nucleus and a neutron, resulting in $17.6\,\mathrm{MeV}$ energy being released [3]. This reaction can be written as

$$\mathrm{D}^+ + \mathrm{T}^+ \rightarrow \mathrm{He}^{2+}(3.5\,\mathrm{MeV}) + \mathrm{n}\,(14.1\,\mathrm{MeV}), \tag{1}$$

where n is the neutron, and the energies show the distribution of the kinetic energies [4]. The D-T fusion is preferred to normal hydrogen fusion or D-D fusion due to a much larger reaction rate coefficient [5].

Building a fusion power plant using this reaction is more easily said than done, however. In order to have these nuclei fuse, they need to collide, which is hindered by the repelling Coulomb forces between the two positive particles [5]. To overcome these forces, the nuclei need to be accelerated to high energies. This is done by heating the plasma, for which various methods are used, such as Neutral Beam Injection (NBI) and Electron Cyclotron Resonance Heating (ECRH) [4]. For more information on heating mechanisms, the reader is referred to chapter 15 of [4].

Now that there is a hot plasma, there is another challenge: creating circumstances in which the D-T fusion can take place effectively. To be able to fuse, the two nuclei obviously need to be close to eachother, since colliding at a distance is impossible. This brings up the need to confine the plasma, even more so since most collissions will be elastic Coulomb collissions, which do not result in fusion. The most common way of confining the plasma is by using magnetic fields. Charged particles will closely follow the magnetic field lines, thereby trapping themselves in the magnetic field. By making the magnetic field shaped like a torus the particles are also prevented from exiting at the end of a tube for instance. The magnetic field is created by magnetic coils, which of course need to be protected from the hot plasma. This once again brings up the need of good confinement.

A major breakthrough in both particle and energy confinement was made by Fritz Wagner at ASDEX in 1982 [6]. While doing experiments with NBI, he found a sudden transition in confinement, which was called H-mode. When the NBI heating increased above a certain value, the confinement suddenly improved [7]. This higher confinement leads to an increase in both density and temperature in the core of the plasma, while the gradients in the core remain the same. This region with increased temperature and density gradients has been named the pedestal region, as it has elevates profiles with respect to the low confinement mode, L-mode [8].

In H-mode the increased gradients in the edge region give rise to magnetohydrodynamic instabilities known as edge localised modes, or ELMs [8]. These ELMs lead to a temporary breakdown of the transport barrier, resulting in a loss of pressure and current from the pedestal region. These breakdowns cause hot particles from the pedestal region to be expelled from the core ending up on the divertor, a region in the tokamak at which exhaust fluxes are directed. [9]. This greatly increases the heat load on the divertor during an ELM. In current devices, ELMs do not destroy the plasma facing components (PFC), but for larger machines like ITER, ELMs will be untolerable. For DEMO, the heat flux out of the plasma needs to be radiated away by impurities for around 90 % to protect the PFCs, even if no ELMs are present.

Over the years a lot of research to protect the divertor, the section of the wall the exhaust is aimed at, has been conducted, for instance on a different divertor configuration [10], and on impurity seeding [11]. Another possibility is to detach the plasma from the divertor, which means reducing the (hot) ion particle flux to the divertor [12]. There are several important factors to establish a detached plasma state, including the plasma-neutral interactions, the volumetric recombination of the plasma and impurity radiation losses [13]. For walls composed of low-Z materials, Z being the atom number, the impurities entering the plasma from the wall play an important role in detachment through radiation [14]. The then cooled plasma near the divertor will experience higher plasma recombination, thereby lowering the particle flux to the divertor. For high-Z walls, such as tungsten, the same effect can be achieved by (dedicated) seeding of low-Z impurities, such as nitrogen [15].

Another interesting observation with regards to the detached divertor was the formation of a local region of high electron density [16]. This region is found to form for a detached inner divertor with a still attached outer divertor combined with sufficiently high heating power. It is located about 20 cm above the X-point in ASDEX Upgrade (AUG), at the inboard side of the torus, near the separatrix. This has led to the region being called the high-field side high density region, or HFSHD. It has been found that the presence of a HFSHD region increases the neutral flux in the SOL. Furthermore, it has been found that nitrogen injections in the divertor region can suppress the HFSHD. This could prove useful, since the HFSHD is suspected to influence the fuelling of the plasma through diffusion or drift-based transport [17].

Detachment of the divertor seems to offer a decent solution for the problem of the divertor, but even during small ELMs there is a possibility of 'burning through' to the divertor, i.e. a transient re-attachment, causing damage despite detachment [13]. Thus other means to either protect the divertor or suppress ELMs are needed. When seeding nitrogen to achieve detachment, it is observed that the divertor radiation can become localised in a small region near the X-point [15]. The X-point itself will be explained more in Section 2.1.1, but for now let's say it is at the boundary between the main plasma and the divertor region. For ASDEX Upgrade, which has a major radius of $R = 1.6$ m, and a minor radius of $a = 0.5/0.8$ m, this region extends over approximately 5 cm in vertical extent. Due to its location and high radiation, this region has been named the X-point radiator, or XPR.

The XPR is observed in H-mode discharges with nitrogen seeding, for different heating powers [15]. The plasma stays in H-mode if operated in the XPR regime. The position of the XPR with respect to the X-point depends on the heating power and the seeding level. More seeding will move the XPR upwards, while more heating will move it downwards. The vertical position of the XPR has been shown to be controllable using a PI controller that regulates the nitrogen seeding. The controller can keep the XPR at a desired vertical position, or move it up to 10 cm into the confined region. While this is being controlled, the XPR radiated power fraction remains close to 100% with respect to the heating power.

When the XPR is located 7 cm or more above the X-point in AUG, it is found that ELMs are suppressed [15]. This ELM suppression comes paired with a slight reduction of plasma density and stored energy, and appears to be an operational regime in between H- and L-mode. In order to maintain ELM suppression, the controller seems to be required for stable operation. Both the radiating aspect and the ELM suppression of the XPR show promise in protecting the divertor in future fusion devices. Though this ELM suppression has been shown experimentally, there is so far no complete understanding as to why this is the case. In order to advance toward understanding of this phenomenon, reproducing an XPR and ELM suppression in simulations is an important step. Efforts have been made using SOLPS, but this code uses only the edge of the plasma [18, 19]. Furthermore, it is not capable of simulating the dynamic time dependent formation of the XPR (or HFSHD). Another important downside with regards to XPR is that it is a 2D code, and hence can't simulate MHD instabilities, such as ELMs. A code capable of these things is JOREK, although it is used in 2D mode in this thesis.

JOREK is a 3D non-linear MHD code designed for realistic toroidal tokamak X-point geometries [20]. It incorporates a discretisation of the full plasma region, up to the PFC. Furthermore, JOREK has extensions for realistic plasma flows, kinetic neutrals and impurities [21]. For a more in depth overview of JOREK, the reader is referred to [20]. These properties make it a suitable tool to investigate the XPR and ELM suppression.

The main focus of this research project is to simulate the formation of an XPR on AUG using JOREK, and to analyse how it influences plasma properties. The research question then is formulated as: *'What physics beyond the MHD model are needed to simulate an XPR in AUG?'*.

As explained previously, the HFSHD and the XPR seem related but typically mutually exclusive. This leads to the question: how are the HFSHD and the XPR related?

Another relevant property of the XPR is the effect it has on the pedestal. A plasma with an XPR appears to be in between H- and L-mode, and the density and energy content in the plasma core decreased somewhat with an XPR present. This gives rise to the question: What is the influence of the XPR on pedestal dynamics? The pedestal region originates from the H-mode, so how does it change during an XPR-discharge? Could the physics in this part of the plasma be the explanation for ELM suppression?

To be able to search for answers to these questions, it is important that the conditions in AUG are reproduced as well as possible in the simulations. This includes the divertor geometry, and the general geometry

of the first wall. Therefore, the first step in this project will be to run 2D H-mode simulations with a realistic geometry. When this is achieved, kinetic neutrals will be added to the simulations, representing the experimental gas puffing. When done properly, this should lead to a detached plasma. Detachment is an important step before an XPR is formed. After detachment, the next step is to introduce nitrogen impurities to the plasma, aiming to achieve XPR formation. To do this properly the nitrogen seeding will mimic the experiments in both location of the gas seeding, as well as seeding rates.

In this work, first some general concepts of nuclear fusion and the tokamak will be explained in Section 2.1. Next up a model to describe the relevant physics will be presented in Section 2.2, after which relevant plasma phenomena will be explored. Then a model predicting access of the XPR will be explained, and a form suitable for this work will be derived in Section 2.3. After this the JOREK model will be explained in Section 2.4, followed by the kinetic particle model coupled to it. After this, first the JOREK plasma simulations done will be discussed in Section 3.1. Then deuterium is added, using the kinetic particle model, followed by nitrogen impurities. The findings of these simulations are presented in Sections 3.2 and 3.3.

2 Theory

In this section, the relevant theory and physics regarding the XPR will be presented. To begin with, a short introduction to nuclear fusion and the tokamak will be given, followed by the magneto-hydrodynamic (MHD) model often used to describe a fusion plasma. Then the focus will shift more towards the XPR itself, taking a look at current understanding and predicted parameters to result in an XPR. Afterwards there will be a short part on MARFEs and how to avoid them.

2.1 The fusion reactor

As mentioned in the introduction, nuclear fusion is a possible way of producing 'clean' energy. The principle is that a deuterium and a tritium nucleus fuse, resulting in a helium nucleus and a neutron, as well as $17.6\,\mathrm{MeV}$, see Equation (1). These reactions can only happen at high enough energies, but that generates an issue: how to confine a hot fusion plasma. There are different ideas on how to do this. First of all there is the inertial confinement [22]. In this approach lasers are used to create a high-energy-density environment in which fusion reactions can take place. The confinement in this case is provided by the plasma inertia. There is also gravitational confinement, which is the confinement in stars.

The way of confining the plasma utilised in this thesis is magnetic confinement, which is currently seen as the best way to develop a fusion reactor. This concept utilises the fact that charged particles closely follow magnetic field lines, as they circle around them [4]. The main components of a fusion plasma are deuterium ions, tritium ions and electrons, and as these all are charged, magnetic fields can be used to confine them. The direction of the gyration with respect to the magnetic field is determined by the charge of the particle. Using a straight magnetic field would result in a cylinder of fusion plasma, but this brings up the next problem: at the beginning of the contained cylinder plasma, a source is needed, and at the other end there is a sink of particles. To solve this problem, the cylinder is bent to the shape of a torus, which means the sink at the end becomes the source at the beginning, thereby creating a closed system.

Using coils to create a torus-shaped magnetic field means that the coils will be placed closer together at the inside than at the outside. This leads to an inhomogenous magnetic field, which is stronger at the inside and weaker at the outside of the torus. This gradient in the magnetic field strength means that at different locations in the orbit of a particle around a field line it will experience different magnetic field strengths. The radius of the gyration, also known as the Larmor radius, depends on $|\mathbf{B}|$ as

$$r_L = \frac{m v_\perp}{|q| B}, \tag{2}$$

in which r_L is the Larmor radius, m is the mass of the particle, $v_\perp$ is the velocity component perpendicular to the magnetic field, q is the charge of the particle, and B is the magnetic field strength [4]. The gradient in the magnetic field strength will therefore turn the circular motion into a drifting motion, the grad-B drift, which is illustrated in Figure 1 [23]. Since the electrons and ions gyrate in different directions, they will drift in opposite directions, resulting in charge separation. This can also be seen from

$$\mathbf{v} = \frac{m v_\perp^2}{2qB} \frac{\mathbf{B} \times \boldsymbol{\nabla} B}{B^2}, \tag{3}$$

which shows the dependency of the drift velocity $\mathbf{v}$ on other quantities [4]. Here $v_\perp$ is the velocity of the particle perpendicular to the magnetic field. Seeing as $\boldsymbol{\nabla} B$ is radially outward and $\mathbf{B}$ is in the toroidal direction, the drift will be in the vertical direction.

The charge separation caused by the grad-B drift gives rise to an electric field, which in turn leads to another drift: the E×B drift. In similar fashion to the grad-B drift, the E×B drift causes the circular motion of the particles to be changed, giving rise to a drift similar to the one shown in Figure 1. This drift is caused by the Lorentz force, and causes the particles to speed up on side of their circular motion, while slowing down on the opposite side [24]. The drift velocity scales with both the electric and the magnetic field strength, and is given by [4]

$$\mathbf{v} = \frac{\mathbf{E} \times \mathbf{B}}{B^2}. \tag{4}$$

As can be seen from Equation (4) the direction of the drift is perpendicular to both fields, and independent of charge, so electrons and ions are drifting in the same direction. Since the electric field is caused by the

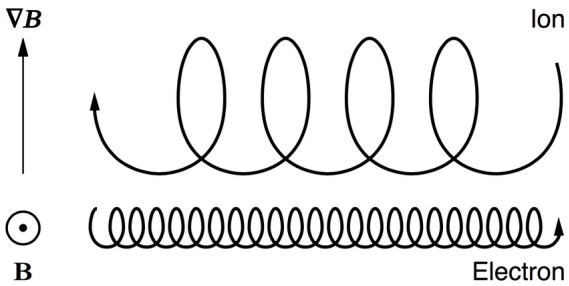

Figure 1: Schematic representation of drift caused by gradients in the magnetic field strength, image from [23].

grad-B drift, the electric field will be oriented in the vertical direction, since the grad-B drift separates the ions and electrons vertically. This means the E×B drift will push the plasma outwards, causing immediate loss of confinement.

Another drift that is present is the so-called curvature drift [4]. It is caused by curvature in the magnetic field, which is clearly present in a torus. the drift velocity is given by

$$\mathbf{v} = \frac{mv_{\parallel}^2}{qB} \frac{\mathbf{r}_c \times \mathbf{B}}{r_c^2 B}, \tag{5}$$

in which $v_{\parallel}$ is the velocity of the particle parallel to the magnetic field, and $\mathbf{r}_c$ is the radius of curvature, pointing radially outward. This drift is once again in opposite direction for ions and electrons, since it is charge dependent. The direction of the drift is opposite that of the grad-B drift, but the two don't typically cancel each other out, and in general the grad-B drift is dominant [24].

The solution to the outward movement of the plasma caused by the E×B drift, is to change the magnetic field from being just toroidal [4]. By adding a poloidal component to the magnetic field, so around the cylinder that was bent into a torus, the ions and electrons can cancel out the vertical electric field without deviating from the magnetic field lines. The magnetic field is changed from purely toroidal to helical. This then raises the next question, how to change the magnetic field such that it has a poloidal component?

In general there are two ways to achieve a helical magnetic field. The first is the stellarator, which uses very advanced magentic coils to create its helical magnetic field [24]. The other option is the tokamak, which drives a toroidal current through the plasma to add a poloidal magnetic field. Both options have advantages and disadvantages. The current for the tokamak is presently generated primarily by a transformer, leading to a pulsed form of operation, and for a long time people have been searching for a way to circumvent this [4, 25]. The stellarator avoids this problem with its complicated magnets, so in theory it can operate in steady state. The complicated magnets of a stellarator have to be mounted very precisly in order to generate the desired magnetic field. The tokamak has a much simpler structure, which is also the reason its development is ahead of the stellarator. Since the XPR phenomenon was found on a tokamak, AUG, the stellarator will not be discussed further here.

As stated above, the tokamak generates its helical magnetic field using a toroidal magnetic field using coils, and by driving a current through the plasma to create a poloidal field. The toroidal field is significantly larger than the poloidal field [26]. The current for the poloidal field is driven by a transformer in the core of the tokamak [4]. This is the reason for the pulsed operation of a conventional tokamak, since a transformer can't generate a steady-state DC current in the plasma. The basic concept of a tokamak can also be seen in Figure 2, which shows the two main components of the magnetic field and the resulting helical magnetic field.

As can be seen in Figure 2, magnetic field lines are no longer closing in one themselves after one toroidal rotation of the plasma. Instead, they typically go round a lot of times before this happens. All of the rotations of a single field line make up a surface, which is called a flux surface [4]. These flux surfaces have 'special' properties which can be very useful for the realisation of a fusion power plant. First of all, since transport along the field lines is unhindered for the charged particles, the pressure and temperature are constant on a flux surface [24]. The flux surfaces are nested toroidally, with the highest pressure at the centre.

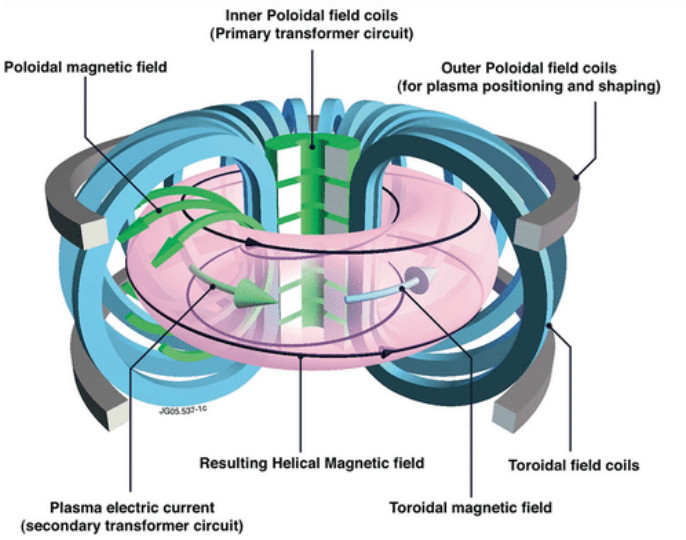

Figure 2: Schematic representation of the important magnetic features of a tokamak, image adapted from [27].

There are some other relevant phenomena regarding the transport of particles on flux surfaces. First of all there is the magnetic mirror effect, which changes the trajectory of some of the particles on a flux surface. This effect can occur when a particle gyrating around a magnetic field line moves parallel to a gradient in de magnetic field strength. The gyration combined with the gradient in the magnetic field causes a Lorentz force to act on the particle, (at least) partly opposite the average velocity of the particle. This means that the particles average velocity will decrease until it reaches zero, after which it will accelerate opposite to its former direction. The point at which this happens is the turning point or reflection point. This effect is called the magnetic mirror effect, and it traps particles in a part of the plasma, rather than letting them flow freely [28]. Combining this with vertical movement caused by gradient and curvature, the projection of a particle trajectory in the poloidal cross section now becomes a banana-like shape [24].

To determine whether particles will be reflected, only the velocity and the magnetic field are required. Particles are trapped when

$$\frac{v_{\parallel}^2}{v_{\perp}^2} < 1 - \frac{B_{min}}{B_{max}}, \tag{6}$$

in which B_{min} and B_{max} are the minimum and maximum value of the magnetic field respectively, and $v_{\parallel}$ and $v_{\perp}$ are the parallel and perpendicular velocity of the particle with respect to the magenetic field respectively [4]. These trapped particles cause an inward drift of electrons, breaking the symmetry over a banana orbit [24]. Also, the banana orbits cause a current known as the Bootstrap current, which is directed in the toroidal direction. When optimised, this can contribute around 80% of the required current in a tokamak, significantly extending the pulse duration.

2.1.1 The divertor region

So far the fusion plasma has been treated as a torus with nested flux surfaces. While this is true for the core, there comes a point moving outward where this is no longer the case. This is due to the divertor, which is used to diminish interaction with the wall of the fusion reactor [29]. Using coils to alter the magnetic field, a magnetic null is introduced in the poloidal magnetic field, which is called the X-point. In the X-point, the field lines (as projected in the poloidal plane) are no longer closed, but cross each other and move outwards. This is illustrated in Figure 3. It should be noted that the actual field lines do not cross here nor anywhere else, at the X-point field lines move only in the toroidal direction, as the poloidal component is zero at the X-point. The separatrix is the boundary between open and closed field lines, so inside the separatrix the flux surfaces are closed, while outside the separatrix they are open. The lower half of the X seen in Figure 3 is called the divertor legs, and they are directed at the divertor strike points, which is the area where they intersect with the wall.

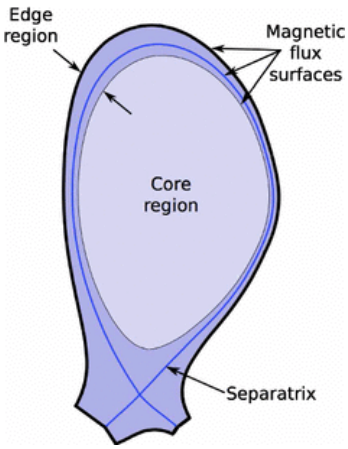

Figure 3: Image schematically showing the separatrix and the X-point in the poloidal cross section, from [30].

If nothing is done to reduce the heat load on the divertor strike points, the heat load can exceed material limits (for all materials), so this is not tolerated [29]. For this reason, some fusion devices operate in detached mode, in which the main plasma is detached from the divertor targets. Detachment is the state of operation in which plasma power and ion fluxes to the divertor surface are limited [31]. In large machines, such as ITER, detachment becomes essential to protect the plasma facing components. Detachment is achieved by impurity seeding in the divertor region, either by sputtering from the wall (in low Z-wall devices) or by actively seeding in impurities (for high-Z wall devices). The presence of impurities near the divertor target leads to an increase in ionisation. This increase in ionisation cools down the plasma near the divertor target, thereby moving up the ionisation front along the legs. Since there now is a cooler region near the divertor, the impurities can no longer be ionised and are excited instead [29]. The excited impurites then radiate away energy when they fall back to a lower energy state, thereby creating a mechanism of reducing the heat load onto the divertor targets.

2.2 Magneto hydrodynamics model

Now that a basic understanding of the geometry of a fusion device has been established, it is time to move towards a convenient way of describing physics in such a plasma. This is commonly done using the magnetic hydrodynamic (MHD) equations. These equations stem from the Boltzmann equation and the Maxwell equations, given by [32]

$$\frac{\mathrm{d}f_\alpha}{\mathrm{d}t} = \frac{\partial f_\alpha}{\partial t} + \mathbf{v}_\alpha \cdot \boldsymbol{\nabla} f_\alpha + \frac{q_\alpha}{m_\alpha}(\mathbf{E} + \mathbf{v}_\alpha \times \mathbf{B}) \cdot \boldsymbol{\nabla}_\mathrm{v} f_\alpha = C_\alpha + S_\alpha(\mathrm{r}, \mathrm{v}, t), \tag{7}$$

$$\boldsymbol{\nabla} \times \mathbf{E} = -\frac{\partial \mathbf{B}}{\partial t}, \tag{8}$$

$$\boldsymbol{\nabla} \times \mathbf{B} = \mu_0 \mathbf{J} + \frac{1}{c^2}\frac{\partial \mathbf{E}}{\partial t}, \tag{9}$$

$$\boldsymbol{\nabla} \cdot \mathbf{E} = \frac{\sigma}{\epsilon_0}, \tag{10}$$

$$\boldsymbol{\nabla} \cdot \mathbf{B} = 0. \tag{11}$$

There are quite some different terms in these equations. First of all it should be noted that the Boltzmann equation (Equation (7)) describes the evolution of a distribution function. Each different type of particle α in the plasma has its own distribution. The mass and charge of each species is given by m_α and q_α respectively. For the kinetic and spatial information, the notation is somewhat more complex, as this is provided by the distribution function f_α. This function gives the number of particles in the volume ($\mathbf{r}$, $\mathbf{r}$+dr), with velocities within ($\mathbf{v}$, $\mathbf{v}$+dv) at time t, as $f_\alpha(\mathbf{r}, \mathbf{v}, t)\mathbf{dr}\mathbf{dv}$. The C_α and S_α terms on the right hand side of the equation together denote the short-range inter-particle interactions[1], sources and sinks of particles per species. Furthermore, in the other equations μ_0 is the vacuum permeability, $\mathbf{J}$ is the current density, c is the speed of light in vacuum, σ is the charge density and ϵ_0 is the vacuum permittivity.

[1] C_α specifically represents the elastic Coulomb collisions.

These equations can be transformed into fluid equations, as shown in [32]. This is done by taking different moments of the Boltzmann equation, which means the equation is multiplied by a function g and then integrated over all velocities. This results in conservation laws for mass ($g = m_\alpha$), momentum ($g = m_\alpha \mathbf{v}_\alpha$) and energy ($g = \frac{1}{2} m_\alpha v_\alpha^2$), given by

$$\frac{\partial \rho_\alpha}{\partial t} + \boldsymbol{\nabla} \cdot \rho_\alpha \mathbf{u}_\alpha = S_{\rho_\alpha}, \tag{12}$$

$$\frac{\partial}{\partial t}\left(\rho_\alpha \mathbf{u}_\alpha\right) + \boldsymbol{\nabla} \cdot \left(\rho_\alpha \langle \mathbf{v}\mathbf{v} \rangle_\alpha\right) - q_\alpha n_\alpha (\mathbf{E} + \mathbf{u}_\alpha \times \mathbf{B}) = \sum_{\beta \neq \alpha} \int m_\alpha \mathbf{v}_\alpha C_{\alpha\beta} \mathrm{d}\mathbf{v} + \mathbf{S}_{m_\alpha}, \tag{13}$$

$$\frac{\partial}{\partial t}\left(\frac{1}{2}\rho_\alpha \langle v^2 \rangle_\alpha\right) + \boldsymbol{\nabla} \cdot \left(\frac{1}{2}\rho_\alpha \langle v^2 \mathbf{v} \rangle_\alpha\right) - q_\alpha n_\alpha \mathbf{E} \cdot \mathbf{u}_\alpha = \sum_{\beta \neq \alpha} \int \frac{1}{2} m_\alpha v_\alpha^2 C_{\alpha\beta} \mathrm{d}\mathbf{v} + S_{E_\alpha}. \tag{14}$$

Here $\mathbf{u}_\alpha$ is the average velocity of the centre of mass, given by

$$\mathbf{u}_\alpha(\mathbf{r}, t) = \frac{\int m_\alpha \mathbf{v}_\alpha f_\alpha(\mathbf{r}, \mathbf{v}, t) \mathrm{d}\mathbf{v}}{\int m_\alpha f_\alpha(\mathbf{r}, \mathbf{v}, t) \mathrm{d}\mathbf{v}} = \frac{\boldsymbol{\Phi}_\alpha^m}{\rho_\alpha}, \tag{15}$$

where Φ_α^m is the mass flux density of species α.

In Equations (12) to (14) the source terms are given by [32]

$$S_{\rho_\alpha}(\mathbf{r}, t) \equiv \int m_\alpha S_\alpha(\mathbf{r}, \mathbf{v}_\alpha, t) \mathrm{d}\mathbf{v}, \tag{16}$$

$$\mathbf{S}_{m_\alpha}(\mathbf{r}, t) \equiv \int m_\alpha \mathbf{v}_\alpha S_\alpha(\mathbf{r}, \mathbf{v}_\alpha, t) \mathrm{d}\mathbf{v}, \tag{17}$$

$$S_{E_\alpha}(\mathbf{r}, t) \equiv \int \frac{1}{2} m_\alpha v_\alpha^2 S_\alpha(\mathbf{r}, \mathbf{v}_\alpha, t) \mathrm{d}\mathbf{v}. \tag{18}$$

The next step is to reformulate these equations, such that they can be solved conventionally by numerical codes, without requiring too much computing power. This requires some assumptions and approximations. First of all, non-relativistic velocities are assumed [32]. This means that Poisson's law can be replaced with the quasi-neutrality condition. Also, the temporal derivative of the electric field in Equation (9) can be neglected.

Since both a fluid plasma background and kinetic ions are considered, the species present are (background) electrons ($\alpha = e$), fully ionised background ions ($\alpha = i$) and kinetic ions ($\alpha = k^0, k^1, ..., k^Z$). For the kinetic ions the k is used to denote the type of ion (for this project this will be D for Deuterium and N for nitrogen), while the superscript denotes the charge of the ion. This means per type of particle there are Z+1 species, from neutral to fully ionised and every state in between. The term background is used here for the standard JOREK plasma, without added neutral particles, since this is added onto the default model.

To reduce the number of unknowns, the electron and ion quantities of the plasma are grouped together as background-plasma quantities. These are defined as

$$\rho_b \equiv \rho_e + \rho_i \approx \rho_i, \tag{19}$$

$$\mathbf{u}_b \equiv \frac{\rho_e \mathbf{u}_e + \rho_i \mathbf{u}_i}{\rho_e + \rho_i} \approx \mathbf{u}_i, \tag{20}$$

$$p_b \equiv p_e + p_i, \tag{21}$$

denoting the background-fluid mass density ρ_b, the centre-of-mass velocity $\mathbf{u}_b$ and the pressure p_b. Furthermore, the electron mass density is considered to be negligible compared to the ion mass density, which holds as long as the kinetic ions are not increasing the electron mass density by a significant amount with respect to the background plasma mass density. Combined with Equation (21) this implies a single temperature model, meaning $T = T_i + T_e$. Also the (absolute) difference in the ion and electron velocities is assumed to be much smaller than the magnitude of these velocities.

The MHD model can then be formulated as a set of normalised equations that describe the time evolution of four different variables [21]. These are the magnetic potential ($\mathbf{A}$), the fluid velocity ($\mathbf{v}$), the mass density (ρ) and the pressure (p). The time evolution of these four variables is describes in Equations (22) to (25). The normalisation is done such that physical constants (such as $\mu_0, \varepsilon_0, k_B$) are not present in these equations, yielding

$$\frac{\partial \mathbf{A}}{\partial t} = -\mathbf{E} - \boldsymbol{\nabla}\Phi, \tag{22}$$

$$\rho\frac{\partial \mathbf{v}}{\partial t} = -\rho\mathbf{v}\cdot\boldsymbol{\nabla}\mathbf{v} - \boldsymbol{\nabla}p + \mathbf{J}\times\mathbf{B} + \boldsymbol{\nabla}\cdot\underline{\tau} + \tilde{\mathbf{S}}_v, \tag{23}$$

$$\frac{\partial \rho}{\partial t} = -\boldsymbol{\nabla}\cdot(\rho\mathbf{v}) + \boldsymbol{\nabla}\cdot(\underline{\mathbf{D}}\boldsymbol{\nabla}\rho) + S_\rho, \tag{24}$$

$$\frac{\partial p}{\partial t} = -\mathbf{v}\cdot\boldsymbol{\nabla}p - \gamma p\boldsymbol{\nabla}\cdot\mathbf{v} + \boldsymbol{\nabla}\cdot(\underline{\kappa}\boldsymbol{\nabla}T) + (\gamma-1)\underline{\tau} : \boldsymbol{\nabla}\mathbf{v} + (\gamma-1)((\mathbf{E}+\mathbf{v}\times\mathbf{B})\cdot\mathbf{J}) + S_p. \tag{25}$$

In these equations the magnetic field is given by

$$\mathbf{B} = F\boldsymbol{\nabla}\phi + \boldsymbol{\nabla}\times\mathbf{A} = RB_\phi\boldsymbol{\nabla}\phi + \boldsymbol{\nabla}\times\mathbf{A}, \tag{26}$$

Where F is the toroidal flux function dependent on ψ. The current density is then described by a simplified version of Equation (9), being

$$\mathbf{J} = \boldsymbol{\nabla}\times\mathbf{B}. \tag{27}$$

The electric field is obtained using Ohm's law (including resisitivity and drift-ordered terms):

$$\mathbf{E} = -\mathbf{v}\times\mathbf{B} + \eta\left(\mathbf{J}-\mathbf{J}_*\right) + F_0\frac{\delta^*}{\rho}\left(\boldsymbol{\nabla}_\perp p_i - \boldsymbol{\nabla}_\parallel p_e\right). \tag{28}$$

In Equations (22) to (25), the different physical quantities are the electric potential Φ, the viscous stress tensor $\underline{\tau}$, the diffusivity tensor $\underline{\mathbf{D}}$, the heat conductivity tensor $\underline{\kappa}$, the ratio of specific heats γ, and the source terms for density, velocity and pressure: $S_\rho, \mathbf{S}_v, S_p$. In the JOREK full MHD model the gauge used is the Weyl gauge, $\Phi = 0$ [20].

While JOREK is capable of solving the full MHD equations, to save on computational cost there is also the option to use a reduced MHD model, which is the case for this work [20, 21]. To do so, fast magnetosonic waves are eliminated, leading to a model with less unknowns compared to full MHD. The reduced model is obtained by using an ansatz-based approach, which assumes that the toroidal component of the magnetic potential is dominant for its time dependent part. Using this approach leads to the following expressions for the parallel and poloidal velocities, as shown in [21]

$$\mathbf{v}_{pol} = (\mathbf{e}_\phi\times\mathbf{v})\times\mathbf{e}_\phi = \mathbf{v}_{E\times B} + \mathbf{v}_{\mathrm{dia,i}}, \tag{29}$$

$$\mathbf{v}_\parallel = v_\parallel\mathbf{B}. \tag{30}$$

For the poloidal velocity this reduces to the E×B effects, since the ion diagmagnetic drift velocity is not used for this work. This leads to

$$\mathbf{v}_{pol} = -R\boldsymbol{\nabla}u\times\mathbf{e}_\phi. \tag{31}$$

The velocity stream function u is defined as $u = \Phi/F_0$ [21]. The expression for the magnetic field used in reduced MHD is

$$\mathbf{B} = \frac{F_0}{R}\mathrm{e}_\phi + \frac{1}{R}\boldsymbol{\nabla}\psi\times\mathbf{e}_\phi. \tag{32}$$

More specifics on how JOREK solves these equations, as well as discretisation are given in Section 2.4. This section also goes more in-depth on the kinetic neutral coupling to the model, which is not standard for JOREK. A complete overview of this is given in [21].

2.3 Plasma phenomena

After taking a look at the tokamak and a way to describe the plasma inside, the next step is to take a look at different phenomena that can be described (and modeled) using the MHD model. First up is one of the main challenges in fusion research: Edge Localised Modes (ELM). A lot of research is focussed at preventing ELMs or their damage to the fusion reactor.

2.3.1 ELMs

ELMs are only present in H-mode plasmas, but due to the better confinement compared to L-mode, switching to the L-mode regime is not a viable solution to this problem. In the introduction it was mentioned that ELMs arise from the increased gradients in the edge region for the H-mode compared to the L-mode. Now let's look in a bit more detail at what causes ELMs.

In the H-mode there is a higher pressure gradient at the edge. This increase in pressure gradient gives rise to the so-called ballooning mode [33]. This is an instability in which the pressure limit is approached [34]. This instability leads to 'fingers' at the outer side of the plasma, which transport heat from the plasma outside to the wall, thus causing a loss of confinement.

Another feature of the H-mode is the increase in plasma current, caused by the 'Bootstrap current'. This increase in current is located mainly in the outer side of the plasma, as shown by figure 4 in [33]. As stated before the Bootstrap current can be beneficial, since it makes up a large portion of the required plasma current. However, the current also leads to so-called peeling modes [35]. These peeling modes are external modes driven by the current near the plasma edge. They are most unstable when a rational surface is located just outside the plasma. A flux surface is rational when both its number of toroidal turns and poloidal turns are an integral number [36]. The ratio of these two is called the safety factor, q or q_s.

The peeling mode and the ballooning mode both have different parameter ranges in which they become unstable [33]. There are also ranges for which both of them are stable. However, a stable region, called the second stability region, is closed off not by one of these two but due to the coupling of both. This leaves a smaller stable space in between these two modes, which limits the pressure and the current at the pedestal, shown in figure 5 of [33]. At low collisionality the current increases, and the peeling mode limits the stability. At high collisionality (and high density) the pressure is the limiting factor, due to the ballooning modes. This theory of coupled peeling-ballooning modes has been shown to provide stability limits that were verified (within uncertainty) by experiments. Numerical simulations have shown that (type I) ELMs are driven by resistive peeling-ballooning modes [37]. The growth rates of the peeling-ballooning modes decrease with lower resistivity, approaching ideal MHD.

2.3.2 High field side high density region

Another plasma phenomenon that is of interest is the high field side high density region, or HFSHD. The HFSHD is characterised by a region of high electron density near the far SOL at the high field side of the plasma [16]. It has been observed for both L-mode and H-mode, and in different devices. In order to observe this region it appears to be important that the inner divertor is (partially) detached, while the outer divertor is fully attached. The HFSHD region forms with increasing heating power, and the local density increase almost tenfold compared to the line averaged plasma density. The HFSHD region is of interest for fusion devices, since it can impact the fuelling of the plasma [17]. Due to its location near the separatrix it can influence the fuelling via diffusion or drift-based transport, which in turn could potentially shift the density profile outwards.

So far the HFSHD region has been linked to high enough neutral concentrations and heating power, and it forms due to strong local recycling and drift-driven transport. Modelling efforts that support the HFSHD region are using ballooning modes to achieve the heatflux required for enough ionisation in this region to obtain the high amount of electrons [17]. The reason this phenomenon is of interest for this project is the fact that is has been shown to diminish with nitrogen seeding. This seems to be the case due to the radiation of power from the SOL by the nitrogen. Since the XPR is formed only with impurity seeding, often nitrogen, it would appear that the HFSHD region and the XPR are mutually exclusive. This means it would be interesting to see if simulations that show a HFSHD region can transition to an XPR with nitrogen seeding. It should be noted that this is dependent on whether or not the HFSHD is present in the simulation, and that this is not the main goal of this project.

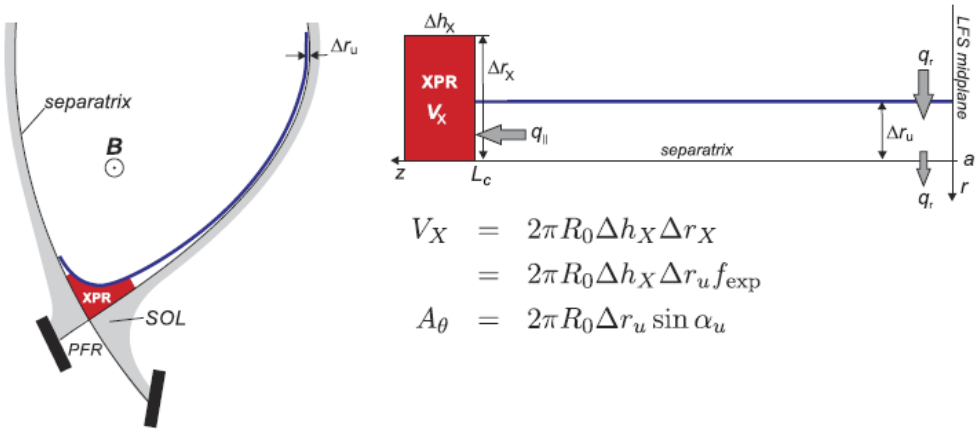

$$V_X = 2\pi R_0 \Delta h_X \Delta r_X$$
$$= 2\pi R_0 \Delta h_X \Delta r_u f_{\exp}$$
$$A_\theta = 2\pi R_0 \Delta r_u \sin \alpha_u$$

Figure 4: Figure showing the relevant geometrical terms for the XPR, including the tube width at the mid plane Δr_u, and the horizontal and radial extent of the XPR volume, Δh_X, Δr_X and V_X respectively. Also labeled are the connection length L_c and the parallel heat flux $q_\parallel$, as well as the effective poloidal area of the XPR volume, A_θ. In the expression for this area the angle α_u is the pitch angle of the upstream field line. This figure was adapted from [18].

2.3.3 X-point radiator

It is clear that nitrogen (or another impurity) is required to obtain the XPR as demonstrated in [15]. However, this experiment does not fully cover why or how an XPR is formed. This is discussed elaborately by Stroth et al [18]. Tied in with this is a MARFE[2], which can be seen as the instable cousin of the XPR. It is also a relatively cold plasma volume with high radiation, but not stable, where the XPR can be controlled to be stable. The MARFE will be discussed more later on, for now the focus will first be on the XPR.

The XPR can best be described as a small plasma volume located slightly above the X-point which is relatively cold (around 1 eV) and is strongly radiating due to impurities in the volume [18]. This is true when an XPR is formed, but this is not how it forms. The formation of an XPR is dependent on several factors. In order to reach a regime in which nitrogen can start to radiate (around 20 eV), the XPR volume needs to be cooled in some way. This means that the power into the volume needs to be smaller then the outflow. In order to describe this, first a geometrical overview is needed.

To determine the heat going into the XPR volume V_X a flux tube connecting the volume to the outer midplane is considered. This tube is depicted in Figure 4 as the region in between the separatrix and the blue line. This blue line is based on observations from experiments, and can be interpreted as the first field line that lies above the XPR at the X-point. In the schematic on the right side of this figure the different geometric quantities are labeled. The width of the flux tube at the outer midplane, the height of $\psi_N = 0$ at the low field side (LFS), is labeled Δr_u, and the width of the tube at the XPR is labeled Δr_X. Using these two quantities, the flux expansion can be expressed as $f_{\exp} = \frac{\Delta r_X}{\Delta r_u}$. The horizontal width of the XPR volume is labeled Δh_X, and the effective poloidal area is labeled A_θ. The pitch angle of the upstream field line α_u can be expressed as $\sin \alpha_u = \frac{B_\theta}{B} \approx \frac{B_\theta}{B_\phi}$ [18].

Using these geometrical quantities the power conducted into the XPR volume can now be expressed as

$$P_{\text{cond}} = 2\pi R_0 \Delta r_u \sin(\alpha_u)\, q_\parallel \equiv A_\theta q_\parallel. \tag{33}$$

In this equation the expression for A_θ also shown in Figure 4 is used. Here the conducted power takes into account only the parallel heat transport, as the perpendicular heat transport is negligible in comparison. As such the conducted power is expressed as the parallel heat flux through the effective area of the XPR volume. This equation can be improved by using an expression for the heat flux: $q_\parallel = \kappa \partial_z T$ [18]. This expression can be used to write T_X in terms of T_u, resulting in

$$T_{\text{X}} = \left(T_{\text{u}}^{7/2} - \frac{7}{2} \frac{q_\parallel L_{\text{c}}}{\hat{\kappa}} \right)^{2/7} \equiv \left(T_{\text{u}}^{7/2} - \frac{q_\parallel}{\hat{\kappa}_{\text{c}}} \right)^{2/7}, \tag{34}$$

[2] Multifaceted asymmetric radiation from the edge

where $\kappa = \hat{\kappa} T^{5/2}$ is the heat conductivity and $\hat{\kappa}_e = 1820$ W (eV$^{7/2}$ m)$^{-1}$ is the heat conductivity for the electron fluid. Using $\hat{\kappa}_c = 2\hat{\kappa}_e / (7L_c)$ the conducted power can be written as

$$P_{\text{cond}} = A_\theta \hat{\kappa}_c \left(T_u^{7/2} - T_X^{7/2} \right). \tag{35}$$

The other relevant power is the power leaving the XPR volume. This can be split up into two parts, power lost due to charge exchange P_{cx} and power lost due to ionisation P_{ion} [18]. Since initially the temperature at the XPR is still similar to the upstream temperature T_u, line radiation from excited impurities is not yet a relevant power loss. The relevant powers are given by

$$P_{\text{ion}} = n_X n_0 \langle \sigma v \rangle_{\text{ion}} \left(E_{\text{ion}} + T_{e,X} + T_{i,X} - 2T_0 \right) V_X, \tag{36}$$

$$P_{cx} = n_X n_0 \langle \sigma v \rangle_{cx} \left(T_{i,X} - T_0 \right) V_X. \tag{37}$$

Here a subscript X indicates the quantity at the X-point, and a subscript 0 indicates it concerns neutral atoms. Both equations contain a temperature dependent cross section for respectively ionisation and charge exchange, the $\langle \sigma v \rangle$ terms. In order to reach an XPR, the XPR volume needs to cool down to a regime where nitrogen radiation becomes relevant. To cool down this region, the power conducted into the volume needs to be smaller than the power outflow, so

$$P_{\text{cond}} < P_{\text{ion}} + P_{cx}. \tag{38}$$

Before exploring what this means for the formation of an XPR, it is important to have a look at a few of the variables in Equations (36) and (37). In these equations the temperature and density at the X-point are used. Using the fact that the flux tube follows the field lines, the pressure should be constant over the length of the field line, and hence

$$n_X = \frac{T_{e,u} + T_{i,u}}{T_{e,X} + T_{i,X}} n_u. \tag{39}$$

This relates the density at the X-point to that upstream. Using $T \equiv T_i = T_e$ this means that $n_X = \frac{T_u}{T_X} n_u$ [18]. Furthermore T_u is much larger than both E_{ion} and T_0. Combining this with Equations (35) to (38) provides the XPR access condition as defined in [18] as

$$X_A \equiv (2\langle \sigma v \rangle_{ion} + \langle \sigma v \rangle_{cx}) \frac{V_X}{A_\theta \hat{\kappa}_c} \frac{n_0 n_u}{T_u^{5/2}} > 1. \tag{40}$$

Using the definitions of the XPR volume and area as presented in Figure 4 and the definition of the pitch angle described earlier this can be approximated as

$$X_A \approx (2\langle \sigma v \rangle_{ion} + \langle \sigma v \rangle_{cx}) f_{exp} \Delta h_X \frac{B_\phi}{B_\theta} \frac{n_0 n_u}{\hat{\kappa}_c T_u^{5/2}}. \tag{41}$$

From this equation it can be seen that there are not many knobs to turn to access an XPR. The best way to change the value of X_A is to change the neutral density at the X-point, n_0. As can be seen in figure 3 in [18] there is a minimum value required for n_0 in order to cool down enough to access a radiation dominant regime. If there are not enough atoms at the X-point the power losses will be fully compensated by the power conducted into the XPR volume, which results in the stable hight temperature solution. The desired XPR however is the low temperature solution, dominated by impurity radiation losses.

After the low temperature solution has been reached the XPR is presumed to be in a stable regime [18]. This can be understood by looking at the power balance again. If the XPR volume cools down even further, the nitrogen will radiate less, since the temperature is (already) below the radiation peak. This means the temperature will increase again. Should the temperature increase from the stable point, the radiation will increase as well, which in turn decreases the temperature again. When the XPR is in its radiative regime, i.e. its power loss is dominated by the impurity radiation, the importance of the neutrals decreases.

When an XPR has formed there is a chance that it becomes unstable and disrupts the plasma. This phenomenon is called a MARFE [18]. When an XPR is already formed, the transition to a MARFE is triggered by an increase in density. A MARFE can also occur with strong heating of an H-mode plasma. In this case the formation can bypass the XPR. In experiments the XPR is kept stable using a controller.

2.4 JOREK

As mentioned before, the model of choice for the simulations in this thesis is JOREK, a "massively parallel fully implicit non-linear extended magneto-hydrodynamic (MHD) code for realistic tokamak X-point plasmas" [20].The development of JOREK began in 2002, with 'JOREK I' by G.T.A. Huijsmans [38]. It was used for, among other things, looking at the stability of external kink modes and the first nonlinear ELM simulations. Since then JOREK has been continuously developed and extended. Here, a short overview of JOREK will be given in general, and then the most relevant features for this work will be explored in more detail. For a full overview of JOREK the reader is referred to the JOREK overview paper [20].

JOREK uses cubic Bézier finite elements to discretise the poloidal R-Z plane. These are based on Bézier curves, used to define the four edges of a bicubic Bézier patch [39]. These patches can be made in such a way that adjacent patches are continuous in both variable values and gradients across element boundaries to cover the whole region of interest. Together with a cylindrical coordinate system (R, Z, ϕ), where ϕ is oriented clockwise when viewed from the top, this is used to define the grid used for simulations. Although not strictly required for JOREK, the grid used is usually flux surface aligned [20]. This is achieved by first creating an initial grid, on which the equilibrium is calculated. This equilibrium is then used to create a flux aligned grid. The toroidal direction is represented by a Fourier expansion.

For the temporal discretisation, all equations regarding physical quantities are expressed as

$$\frac{\partial \mathbf{A}(\mathbf{u}, t)}{\partial t} = \mathbf{B}(\mathbf{u}, t), \tag{42}$$

where $\mathbf{u}$ is the vector denoting said physical variables. They are discretised in time according to

$$\left[(1+\xi)\left(\frac{\partial \mathbf{A}}{\partial \mathbf{u}}\right)^n - \Delta t\theta\left(\frac{\partial \mathbf{B}}{\partial \mathbf{u}}\right)^n\right]\delta\mathbf{u}^n = \Delta t\mathbf{B}^n + \xi\left(\frac{\partial \mathbf{A}}{\partial \mathbf{u}}\right)^n \delta\mathbf{u}^{n-1}. \tag{43}$$

In this equation $\delta\mathbf{u}^n = \mathbf{u}^{n+1} - \mathbf{u}^n$ is defined as the change of the value of $\mathbf{u}$ for the time step from n to $n+1$. Different schemes for the temporal discretisation can now be selected by setting (θ, ξ) to the appropriate values. For the second order linearised Crank-Nicholson scheme, this is done by setting $(\theta, \xi) = (\frac{1}{2}, 0)$, and for the second order BDF2 Gears scheme, they are set to $(\theta, \xi) = (1, \frac{1}{2})$. Both schemes are commonly used for JOREK simulations [32]. For the simulations with kinetic particles and impurities, a hybrid scheme is used. The kinetic particle orbits are advanced explicitly in between the implicit fluid time steps. The kinetic coupling terms are all explicit.

A standard JOREK simulation starts by initialising a background-fluid state [32]. This can be done by solving the Grad-Shafranov equation to obtain an equilibrium state [20]. When a simulation is continued from previous simulations, this is replaced by loading a state from said previous simulation. In a pure fluid simulation, time steps are then successively performed by solving a large sparse matrix solver, obtained by the finite element approach, while the selected number of time steps were completed.

For a simulation with kinetic perticles, the procedure becomes a bit more elaborate. First thing to note is that there are two different time-step-sizes involved now. There is the fluid time step, which relates to time in SI units as

$$\Delta t = \Delta\tilde{t}\sqrt{\mu_0\rho_0}, \tag{44}$$

where $\Delta\tilde{t}$ is the time step size in JOREK units, and ρ_0 is the mass density at the centre of the plasma in kg m^{-3}, which is defined by the input parameters of the simulation [40]. The time step size can be increased or decreased in the input file using this time unit as a basis. Next up is the kinetic time step, which is a direct input parameter. When choosing this parameter it is important that several steps are performed within the time of one ion cyclotron gyration to obtain converged results. The kinetic step is significantly smaller than the fluid time step. In this thesis, the kinetic time step is 1×10^{-8} s, while the fluid time step is 6.258×10^{-7} s.

A simulation with kinetic particles also starts by initialising a background-fluid state [32]. Successively the kinetic particles are initialised. This can be done by sampling based on background-fluid variables, by loading a previous save state, or over time by prescribed sources. Since the kinetic time step is smaller

than the fluid time step, several kinetic time steps are performed, until the sum of the steps is the size of one fluid time step[3]. Then all the feedback terms from the kinetic model for the background-fluid model are calculated and projected onto the finite element grid. Now the background-fluid time step is performed, which starts at the time where the kinetic model started, and finishes where the kinetic model left off, meaning both parts of the hybrid model are now at the same point in time. Additional particles are initialised if a particle source is involved. Then the kinetic time stepping commences with the updated fluid fields, and the process is repeated.

2.4.1 Kinetic particle model

The kinetic particle model is used in tandem with the background-fluid model, both providing feedback terms to the other. In this section the kinetic particle model will be explored a bit more in depth, since it is this part that is relevant to the simulation of nitrogen atoms and ions as well as deuterium neutrals, all of which are treated as kinetic particles in this thesis.

The kinetic particle model incorporates different physical interactions regarding the neutral particles [21]. First of all there are the interactions between the background plasma and the neutrals. This includes electron-impact ionisation, effective radiative recombination reactions, and charge exchange (CX) between neutral and ionised particles.

The kinetic particle model uses the so-called Boris method to follow the orbits of particles [21, 41]. This is true for both the (R, Z, ϕ) space as well as the local (s, t, ϕ) space of the cubic Bèzier elements. The Boris algorithm is the standard when it comes to pushing a charged particle in an electromagnetic field through time steps, since it is energy conserving up to machine precision. Specifically when the resulting force acting on the charged particle is the Lorentz force. The Boris algorithm solves the discretised equation of motion to obtain the next phase space coordinate of the particle.

The interactions of the neutral particles are relevant to the background-fluid model. The ionisation of neutral deuterium provides a source for ions and electrons forming the background plasma described as fluid, as well as momentum and energy sources [21]. To be able to take these into account in the fluid model, the discrete particle distribution needs to be converted to the continious description of the finite elements. This is explained more by Korving et al. in [21].

The interaction between the background-fluid and the kinetic particles is done via so-called coupling terms [21]. These are based on the continuity equation, momentum equation and energy equation for ionisation and recombination. For the continuity equation the change in ions and electrons is the reaction rate for ionisaton minus that for recombination. For the neutrals this is the other way around, so the reaction rate for recombination minus that for ionisation. The reaction rate coefficients are obtained from the open ADAS database.

For the momentum equation this already is a bit more complicated than for the continuity equation. The conservation equation of momentum (for JOREK) is written as

$$m_\alpha n_\alpha \left(\frac{\partial \mathbf{v}_\alpha}{\partial t}\right)_{i,r} = \frac{\partial m_\alpha n_\alpha \mathbf{v}_\alpha}{\partial t} - m_\alpha \mathbf{v}_\alpha \left(\frac{\partial n_\alpha}{\partial t}\right), \tag{45}$$

where the subscript α is used to distinguish between ions, electrons and neutrals [21]. Here the only left hand side of Equation (23) is considered, as well as the source terms of interest. The second term on the righthandside of Equation (45) is to keep the equation conservative, and it takes into account the source or sink of the particles, as described by the continuity equation.

The energy equation, in its desired form for JOREK, is given by

$$\frac{\partial E_\alpha}{\partial t} = \frac{\partial \left(\frac{1}{2} m_\alpha n_\alpha v_\alpha^2 + \frac{n_\alpha T_\alpha}{\gamma - 1}\right)}{\partial t}, \tag{46}$$

$$\frac{\partial \left(n_\alpha T_\alpha\right)}{\partial t} = (\gamma - 1)\left[\left(\frac{\partial E_\alpha}{\partial t}\right) - v_\alpha m_\alpha n_\alpha \frac{\partial v_\alpha}{\partial t} - \frac{1}{2} m_\alpha v_\alpha^2 \left(\frac{\partial n_\alpha}{\partial t}\right)\right]. \tag{47}$$

[3] The input kinetic step size is altered such that an integer number of steps fit one fluid time step.

Here the α again distinguishes between ions, electrons and neutrals. The energy equation has a contribution from both the ionisation and recombination, a full overview of which can again be found in[21].

To couple back the correct information regarding the kinetic particles to the JOREK fluid plasma, the right moments and coupling schemes are needed [21]. The three moments required for the coupling are mass density, momentum and energy. The effects of the interactions between the plasma and the neutral particles are summed up into one source term per equation. In JOREK form, this gives

$$\frac{\partial \rho}{\partial t} = \tilde{S}_\rho = S_\rho, \tag{48}$$

$$\rho \frac{\partial \mathbf{v}}{\partial t} = \tilde{\mathbf{S}}_v = \mathbf{S}_v - \mathbf{v} S_\rho, \tag{49}$$

$$\frac{\partial (\rho T)}{\partial t} = \tilde{S}_E = (\gamma - 1)\left(S_E - \mathbf{v} \cdot \mathbf{S}_v + \frac{1}{2} v^2 S_\rho \right). \tag{50}$$

These equations are formulated for kinetic neutrals, but can be expanded to also include impurities. This is done by splitting the momentum source term into a neutral source and an impurity source, such that

$$\rho \frac{\partial \mathbf{v}}{\partial t} = \tilde{\mathbf{S}}_{v,n} + \tilde{\mathbf{S}}_{v,i}. \tag{51}$$

In these source terms all the relevant physics is included. The ionisation and recombination of kinetic neutrals are included in S_ρ. Impurities are not considered here, since ρ is the mass density, and the impurities are not lost to or added from the fluid plasma. The electron loss due to impurity ionisation is negligible, since this is a mass density. The momentum source(s) include the charge exchange of the kinetic neutrals, collisions of impurities, as well as ionisation and recombination. The energy source term includes the radiation of neutrals and impurities.

It is important to note that the assumption of $n_i = n_e$ holds when only hydrogen isotopes are considered, since these atoms have only one electron. Ionising such an atom yields one ion and one electron. However, for higher atomic numbers this is no longer necessarily the case, since these atoms can lose multiple electrons. The current model does not use the electrons 'lost' by the neutrals and impurities, which is an assumption based on low impurity concentrations. However, when higher impurity concentrations are involved this assumption may not hold.

To allow for computationally viable simulations, not every physical particle can be simulated individually. Rather, so-called superparticles or markers are used, each of which represents a multitude of actual particles [42]. The number of physical particles it represents is expressed by the weight of the superparticle. All calculations involving a superparticle are done once for the type of particle it is and then multiplied by the weight of the superparticle. This requires separate superparticles for different types of particles. The weight of a superparticle can be reduced by ionisation of its particles, and if the weight drops below a critical value the superparticle is removed [21].

Kinetic particle simulation set-up

In this work the kinetic particles are initialised to represent a particle source. The particle distribution is centered around a given location. In this case the locations are two areas in the private region, the location of which can be seen in Figure 5. The particles are initialised with an upwards velocity to replicate a gas puff.

In this work two different types of particles are used, neutral deuterium and nitrogen. The deuterium is already present in the plasma, whereas the nitrogen is an impurity species. Both are initialised at the same two locations. The different tuneable variables that are associated with the puffing are:

- Start time: the time (in JOREK units) at which the puffing will start to increase to the desired puff rate.
- Final puff rate: the target rate at which the neutral particles are puffed in atoms per second.

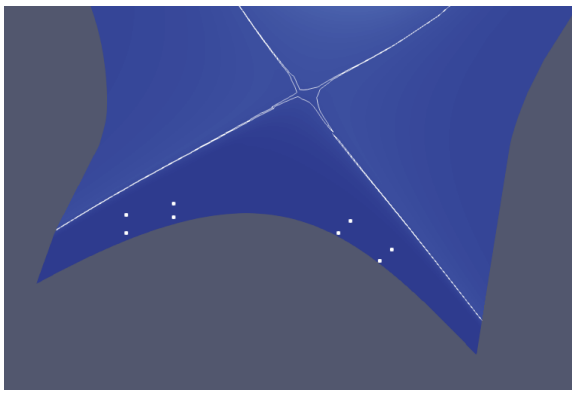

Figure 5: Image showing the location in which sources representing the deuterium and nitrogen puffing are modelled. The two locations are visible as rectangles each consisting of four points. The white lines show where the plasma separatrix and X-point are located.

- Initial puff rate: the rate at which neutral particles are puffed prior to reaching the start time, also in atoms per second.

- The ramp up time: the time in which the puff rate will be changed from the initial puff rate to the final puff rate, in seconds.

These variables can all be set individually for both species. The locations for the puffs can also be set different, but that has not been done for this work.

3 Results

In this chapter the results of this project will be shown. To simulate an XPR, first the simulation is set up with a JOREK fluid simulation. This simulation is started from equilibrium data from the experiment described in [15]. Using this as a starting point, neutral deuterium is added to the simulation, using the kinetic particle model, described in Section 3.2. Lastly, nitrogen is added to the simulation, the results for simulations with both deuterium and nitrogen included will be presented in Section 3.3.

3.1 Base simulation without neutral particles and impurities

In order to keep the simulations close to the experiment which showed an XPR [15], the simulations were started from an experimental equilibrium reconstruction, for which a suitable simulation grid needed to be constructed, which is shown in Figure 6.

Since the area of interest is the X-point and the divertor region, the grid is designed to have a good resolution in these areas. This is achieved by increasing the number of grid lines in the divertor region, as well changing the density of the grid lines to be higher radially at the edge and poloidally towards the X-point. Additionally, in the private region, the density of the grid lines is increased close to the strike lines, since high gradients are expected in these areas. The increased resolution allows to resolve physical structures accurately an thus avoid the formation of unphysical negative densities or temperatures. These could be caused by 'overshoots' in the finite element representation.

The simulation itself was started from equilibrium data from the actual experiment, as described in [15]. To keep close to this experiment, the next step was to find the correct input parameters for the heating of the plasma. In the experiment, this was $10\,\mathrm{MW}$. The energy source in the simulation is centered at $\psi_n = 0.95$, and is ramped down over a width of $\sigma = 0.05$.

Once the simulation matches the experimental heating power, the background transport coefficients needed to be determined in a way to maintain the initial profiles. These coefficients define the parallel and perpendicular transport coefficients in general, as well as some geometrical properties. Specifically the transport coefficients in the pedestal region, as well as the width of the pedestal, the sharpness of the transition from core to pedestal region, starting value of the pedestal region in ψ_N and the diffusion in the SOL are provided.

The particle source for the simulation was set at $\psi_n = 0.9$. To mimic sputtering from the walls, also a Gaussian particle source was added. The location and standard deviation were set to $\psi_n = 1.03$ and $\sigma = 0.05$. This additional source was necessary to maintain the transport in the SOL as provided in the input equilibrium.

The final state of the plasma background simulation can be seen in Figure 7. These figures show the final electron density and temperature profiles of this simulation. In Figure 7b it can be seen that the temperature is higher on the strike lines than in the surrounding area, as expected. The slightly negative bottom of the temperature range is negligible compared to the relevant temperatures, and is of course not physical.

Since the plasma background simulation is initialised from an equilibrium, it is important to see whether there are large differences between the beginning and end of this simulation. Too strong difference indicates that the plasma is different from the experimental data, which could lead to differences later in the simulations.

Figure 8 shows the density and temperature profiles over a line at the beginning and end of the simulation. While not identical, these lines are very similar. The main differences are a slight decrease in density outside of the main plasma, and a slightly higher core temperature. The temperature gradient in the plasma and the drop outisde the plasma are similar, and for both density and temperature the sharp transition is located at the same location at the beginning and end of the simulation.

The final results of this simulation are used as a starting point for the simulations with deuterium puffing.

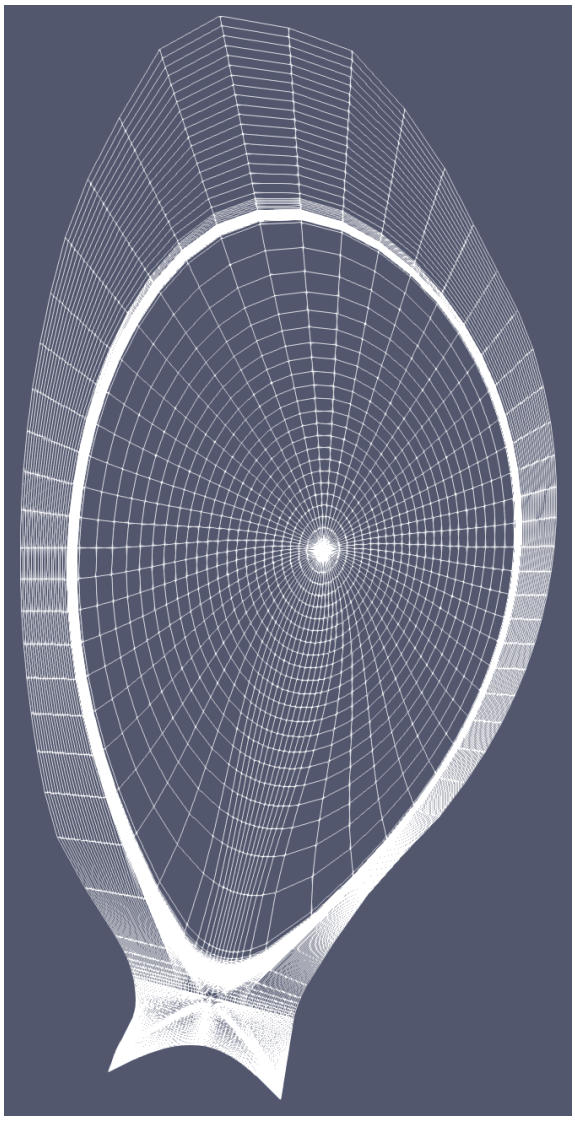

Figure 6: Representation of the final version of the grid used for the simulations. Key points of the grid are the X-point and the divertor region. This image clearly shows the increased resolution in these areas.

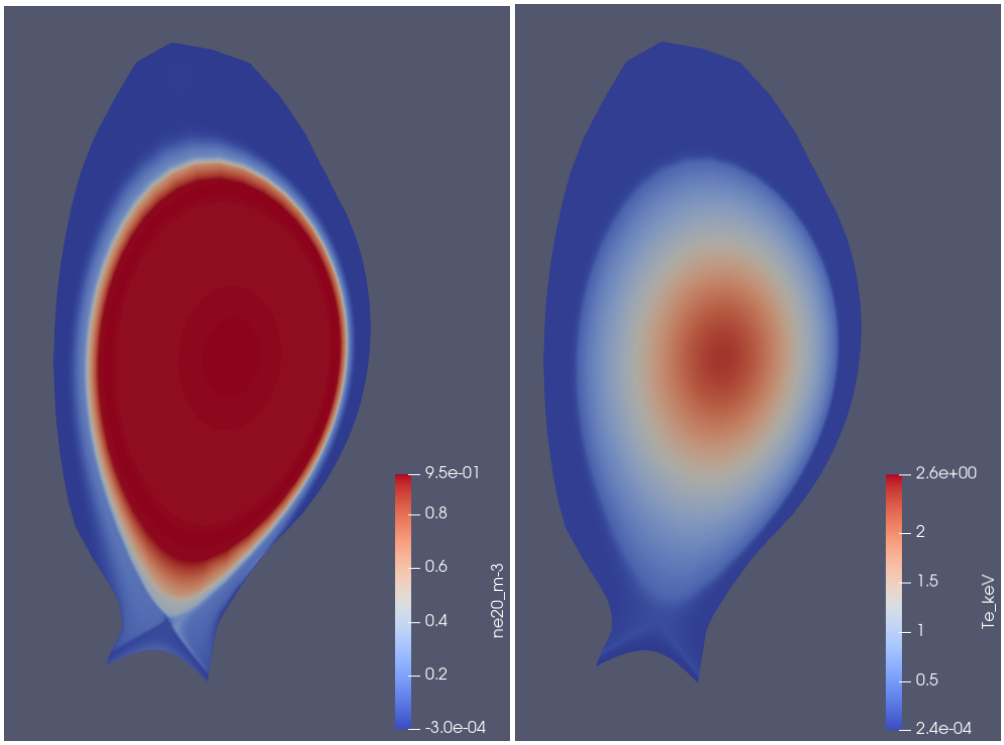

(a) (b)

Figure 7: Images of (a) the density and (b) the temperature at the end of the plasma background simulation.

3.2 Kinetic neutrals

Once the equilibrium of the background plasma was obtained, the next step was to add a deuterium puff. As shown in Figure 5, the deuterium is puffed from two locations within the private region. Additionally there is a static puff near the top of the vessel, outside of the centre plasma. This puff has a lower magnitude, 5×10^{20} atoms per second, than those in the private region, and is there to compensate for a change in the fluid source. In the plasma background simulation, there was a particle source, which is now disabled since there is deuterium puffing. Without the puffing at the top of the vessel, this resulted in negative densities at the top, since the puffing reaches this location only after a long time. The addition of the extra deuterium puff solves this problem almost completely, and the residual negative densities are negligible and far away from the area of interest.

The deuterium (super)particles are initialised with a vertical velocity, to mimic a gas puff. When the simulation is started, the puffing rate for the deuterium is 5×10^{20} atoms per second, which almost immediately is increased to a final puffing rate of 2.15×10^{22} atoms per second. This increase is done linearly in 5×10^{-4} sec.

The density of the neutral deuterium at different times during the simulation can be seen in Figure 9. In these images, the initialisation locations are clearly visible. Over time, the highest deuterium concentration is not found at these locations but at the divertor wall, just below the strike point. When the simulation is done increasing the puffing rate to its desired value, the neutral deuterium profile is constant, as can be seen from Figures 9e and 9f. The profile does not (visibly) change between these two points in time, indicating that plasma with deuterium puffing is now approximately in steady state, for over a millisecond.

The electron density profile of the plasma is not changed for the most part after the deuterium puffing. Mainly the divertor region is influenced by the addition of the hydrogen isotope. The puffed deuterium is ionised in the divertor region, which (locally) increases the electron density significantly. This is well visible in Figure 10, where the divertor region shows a significant increase in electron density.

The temperature for the core plasma is, much like the electron density, mostly unchanged when deuterium puffing is added, as visible in Figure 11. The private region is cooler than prior to the deuterium puffing, and the strike lines are clearly visible, appearing as a boundary between the private region and the rest of

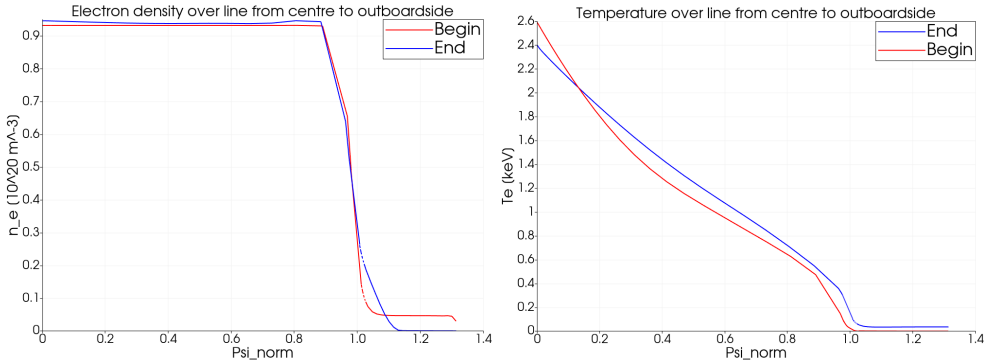

(a) (b)

Figure 8: Images of (a) the density and (b) the temperature at the beginning and the end of the plasma background simulation, plotted over ψ_n. The density is given in $10^{20}\mathrm{m}^{-3}$ and the temperature is given in keV. The line over which these graphs are taken starts at the centre of the plasma and moves towards the outside of the plasma, horizontal in Figure 7 (i.e. the outer midplane).

the volume. The cooling of the private region is logical, since a lot of cold (neutral) particles were added, which require energy to ionise.

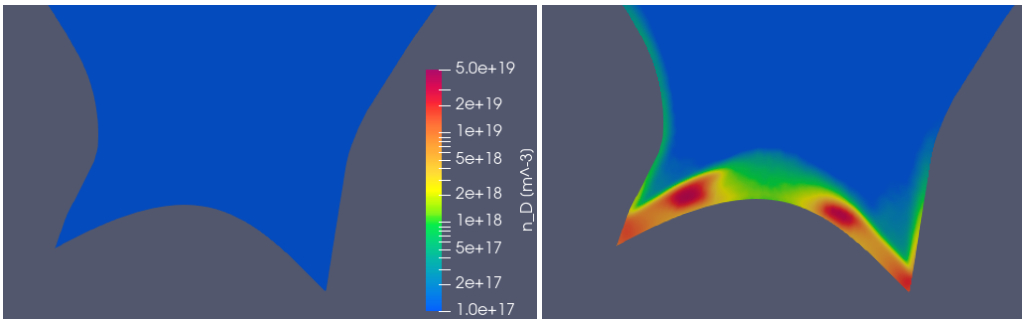

(a) t =7.51 ms (b) t =8.14 ms

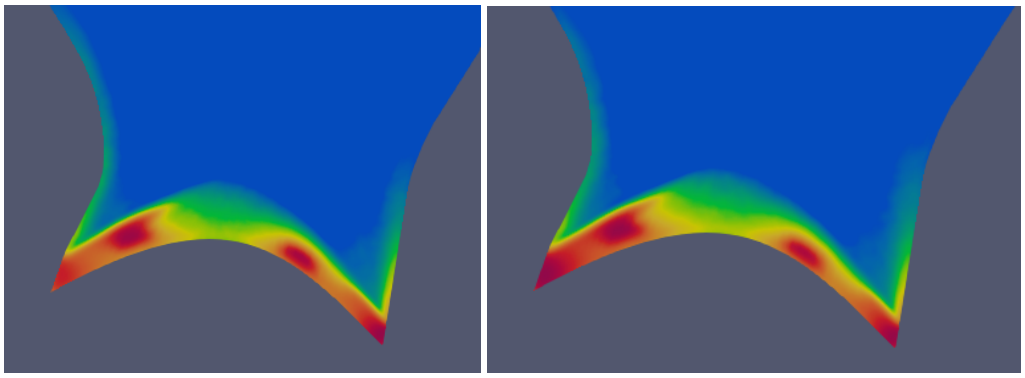

(c) t =8.76 ms (d) t =9.39 ms

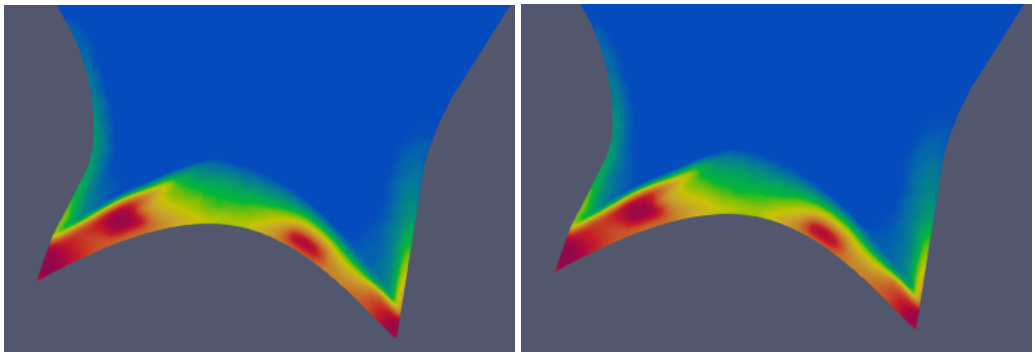

(e) t =10.02 ms (f) t =11.27 ms

Figure 9: Images showing the neutral deuterium density during the simulation at different times. Initially the density is just increasing, but after some time this is almost stopped due to ionisation reducing the amount of neutral deuterium at almost the same rate as neutral deuterium is puffed in.

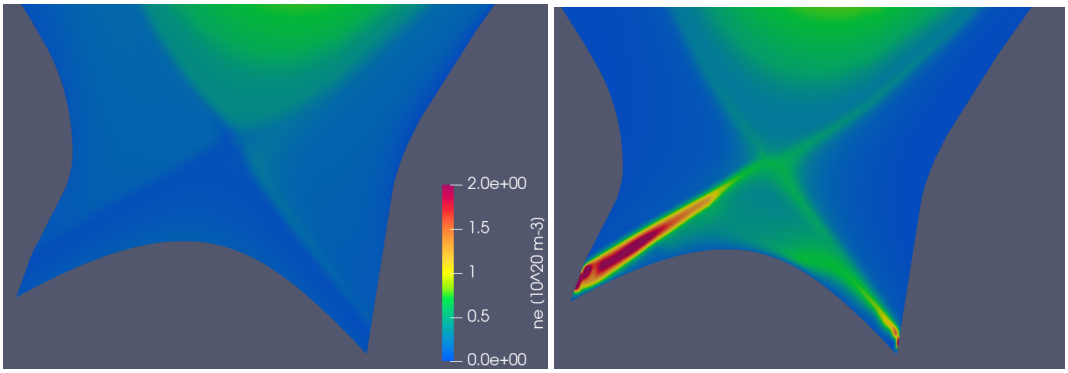

(a) (b)

Figure 10: Images showing the electron density profile at (a) the start of the deuterium puffing and (b) at the end of the simulation.

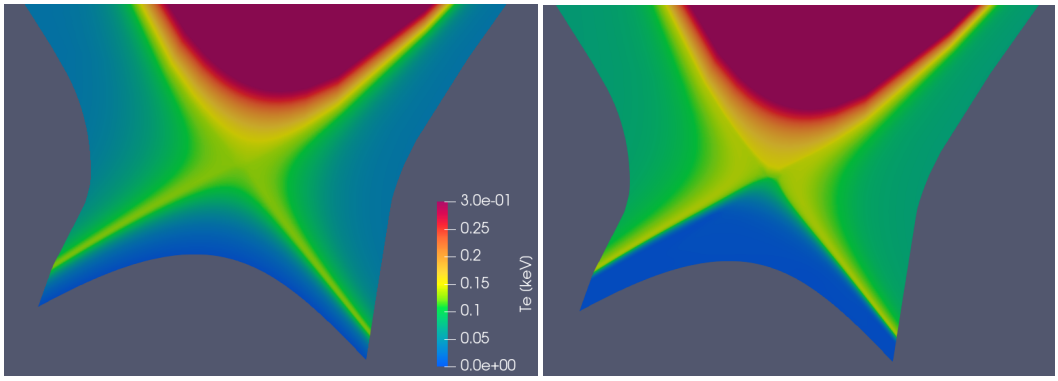

(a) (b)

Figure 11: Images showing the temperature at (a) the start of the deuterium puffing and (b) at the end of the simulation.

3.3 Impurities

After the deuterium puffing the next step towards the XPR is to puff nitrogen in the private region. This is done from the same location as the deuterium puff, which is continuing at the same rate of 2.15×10^{22} atoms per second. The nitrogen puff is started from 0 atoms per second, which is different from the deuterium, which had a nonzero puffing rate prior to ramping it up. This was to mimic the fuelling of the plasma, but for nitrogen this is not necessary.

The nitrogen puffrate starts at zero and is increased over a time of 5×10^{-3} s. Several different puffrates for nitrogen were tried, with differing degrees of success. Most of the simulations resulted in a termination due to numerical instabilities, which couldn't be resolved on the timescale of this thesis project. However, a puffrate of 1×10^{23} atoms per second showed promising results (before also terminating). This puffrate is a factor 10 higher than those from the experiment as described in [15]. The results shown below are all from the simulation with this puffrate.

One of the diagnostics used to analyse the dynamics of the simulation shows the nitrogen density distribution in the entire plasma, including both neutral and charged nitrogen. This diagnostic is very useful, since it shows the distribution of nitrogen throughout the simulation. Initially the nitrogen is mainly concentrated at the puffing locations, as seen in Figure 12a. After some time this shifts towards the areas just below the strikepoints, where a lot of the nitrogen appears to pile up. Simultaneously, the nitrogen starts to travel around the whole plasma, clearly visible in Figures 12b to 12d. This movement is likely due to E×B drifts.

The high concentration of nitrogen present in the outer leg (Figure 12c) starts to move upwards, following the edge of the plasma core. This significantly increases the amount of nitrogen surrounding the plasma core. When this movement has completed a full poloidal turn around the plasma two new phenomena arise. First of all, the concentration of nitrogen at the inner strike point is increased over a larger region than before, see Figure 12e to Figure 12f. Additionally, the area just above the X-point, which previously had almost no nitrogen, now also contains a significant amount of nitrogen, already visible in Figure 12f. The amount of nitrogen keeps increasing in these two regions, clearly visible from Figure 12g.

A really interesting part of the nitrogen distribution during the simulation are the two loops around the plasma that are present. In the first loop, the nitrogen travels around the core, and then flows into the inner leg. The second, more visible loop, consisting of the large amount of nitrogen present in the outer leg, not only goes towards the inner leg but also towards the X-point region. This difference is visible in Figure 12d and Figure 12e, where the latter figure shows more nitrogen looping around than the former. Due to a change in the electric potential when comparing the first loop to the second, as well as more nitrogen looping around, the distribution is different. In the first loop almost no nitrogen moves towards the X-point, but in the second loop a significant part of the nitrogen ends up at the X-point.

The transport of the nitrogen is also shown schematically in Figure 13. One important aspect of this transport is the fact that most of it follows the contourlines of the potential, which are also shown. This is logical, since the ionised nitrogen is charged, and therefore exhibits E×B dift.

The radiation of nitrogen is another diagnostic that is available. From this it can be seen that at $t = 13.1$ ms there is some radiation on the strikelines, see Figure 14a. After that, for a while no significant radiation is observed (Figure 14b). Then, when the nitrogen is spread as shown in Figure 14c, there is some radiation around the X-point, Figure 14c. This increases in a short time to the radiation seen in Figure 14d. The increase in radiation seems to be correlated to the concentration of nitrogen around the X-point, since this also increases in the same timeframe.

The inclusion of nitrogen impurities to the simulation is not only relevant for a possible XPR. Another expected effect of adding impurities to the plasma is detachment, as explained in Section 2. In this simulation indeed detachment is observed, visible in Figure 15. Initially not much is happening, until around $t = 13.3$ ms, when the SOL starts to cool down due to radiation in the divertor legs. Then the outer leg cools down drastically, as shown in Figure 15b. When the outer leg is cooled down and detached, the SOL cools down counter-clockwise around the plasma core, until it reaches the inner leg, which is still (relatively) hot at this point. When the cold front reaches the inner leg this too begins to cool down, until the entire SOL is in the few eV range and the plasma is fully detached. This does not happen in the simulation without nitrogen, since the impurity radiation is the mechanism to cool down the legs. Experiments typically show the

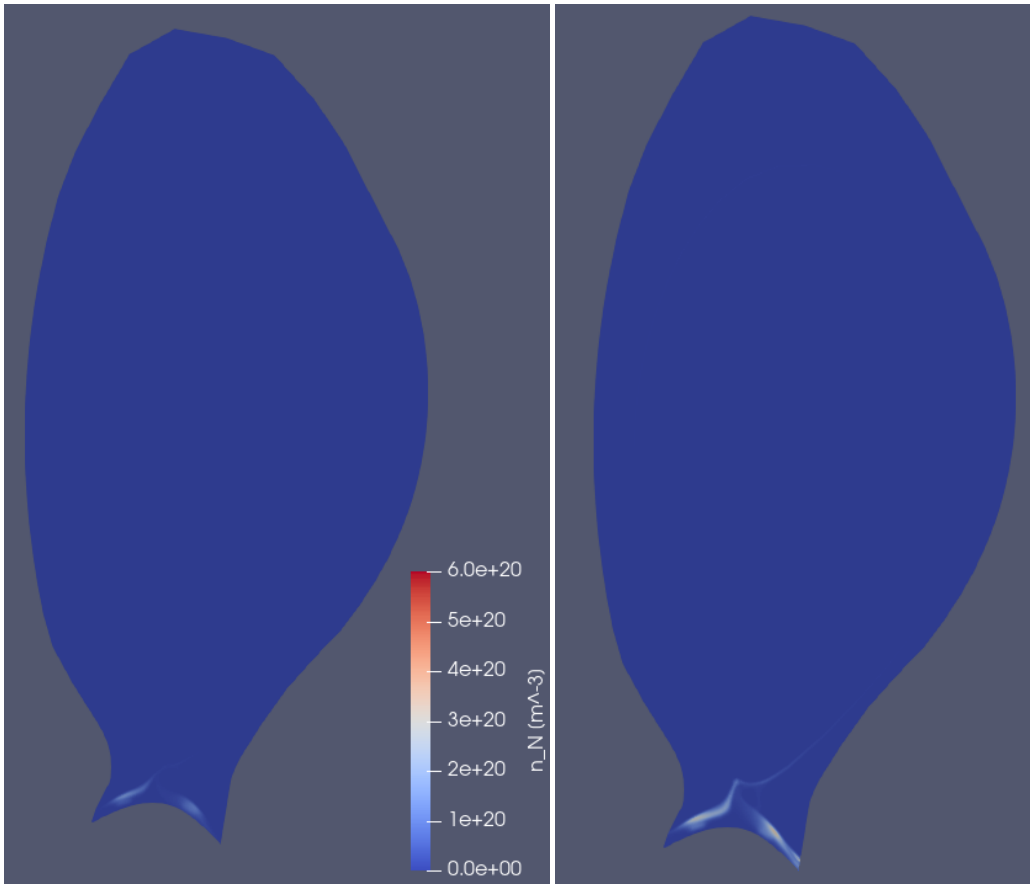

(a) t =12.0 ms (b) t =12.7 ms

inner leg detaching first. In this case, the difference can be explained by the high concentration of nitrogen in the outer leg compared to the inner leg, see Figure 12c.

When monitoring the temperature and density throughout the simulation, it becomes clear that the pedestal is mostly maintained. At the outboard midplane the change is minimal. Most change is seen around the X-point, which can be explained by the radiation just above the X-point. This shifts the pedestal slightly inward. This change is less obvious than the change that could be expected. In experiments ([15]), the XPR was paired with a reduction of the confinement properties, putting the XPR plasma just below H-mode. This change was suspected to be due to changed pedestal transport, but this is not seen in the simulation. This change might become visible in a longer simulation.

3.3.1 Access parameter

In Section 2 the access parameter for an XPR was explained and derived, resulting in Equation (41). Using this equation, the access parameter was calculated in the region of interest. To do this, the temperature and density were taken upstream over a line, and then matched to the points of interest around the X-point using their ψ_n coordinate. This is done such that the upstream values used are in the same flux tube as the point of interest in the X-point region. Furthermore the ionisation and charge exchange rates were determined from a linear fit, since the regime of interest exhibits a linear dependence on the temperature.

There are a few constant values in this formula, the first being the heat conductivity for the electron fluid $\hat{\kappa}_c = 1820$ W (eV$^{7/2}$ m)$^{-1}$. Another value is $\Delta h_X = 4.77 \cdot 10^{-2}$ m. This second parameter is the size of the XPR volume in the toroidal direction, see Figure 4, which is not inherently constant. However, since the analysis is done for many different locations and through the entire simulation, it is not possible to measure the size of a radiating volume seperately for each point. Therefore the toroidal length of the final radiating volume was used for all calculations. The measured value is in the same regime as the value used by Stroth et al. in [18]. The poloidal and toroidal magnetic fields are also taken as a constant, and are calculated using the relevant input parameters, being $B_\phi = 1.751$ T and $I = 0.723$ MA, yielding $B_\theta = 0.17$ T.

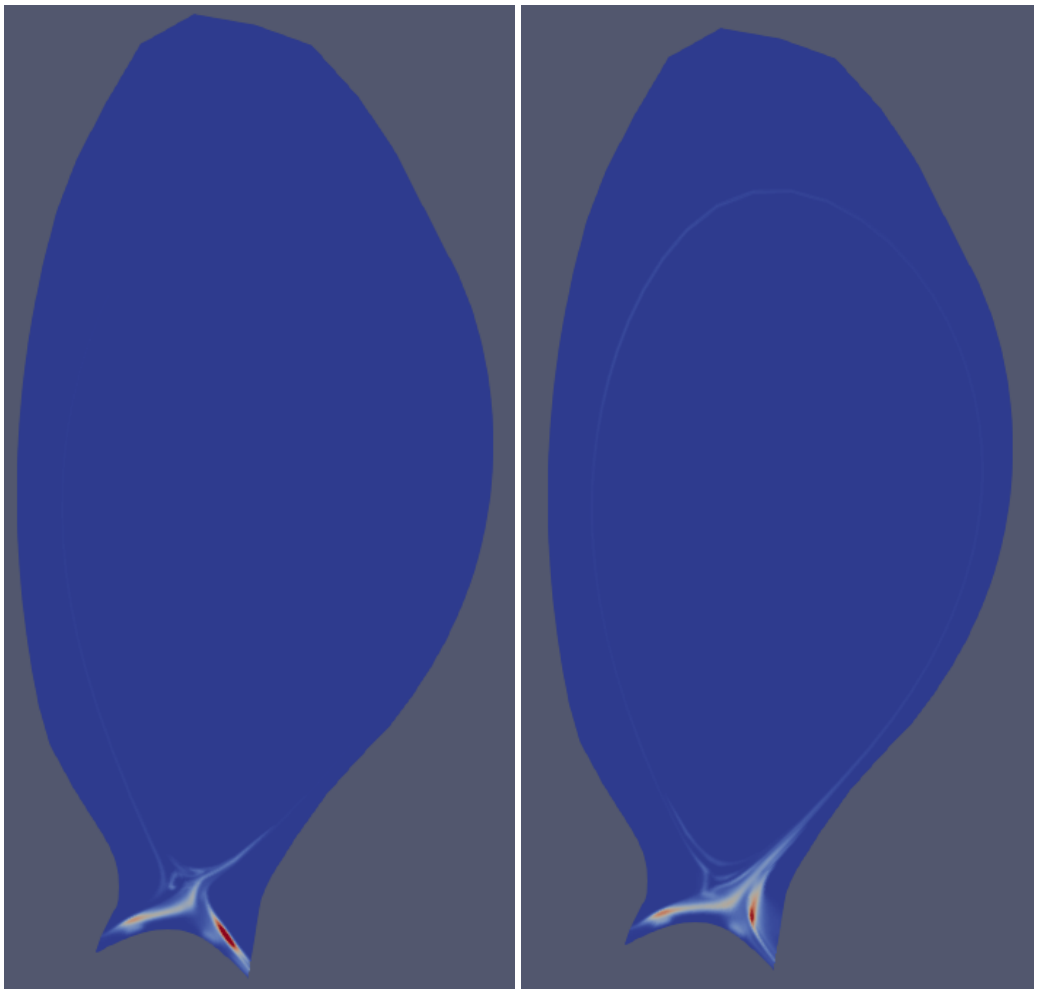

(c) t =13.3 ms

(d) t =13.8 ms

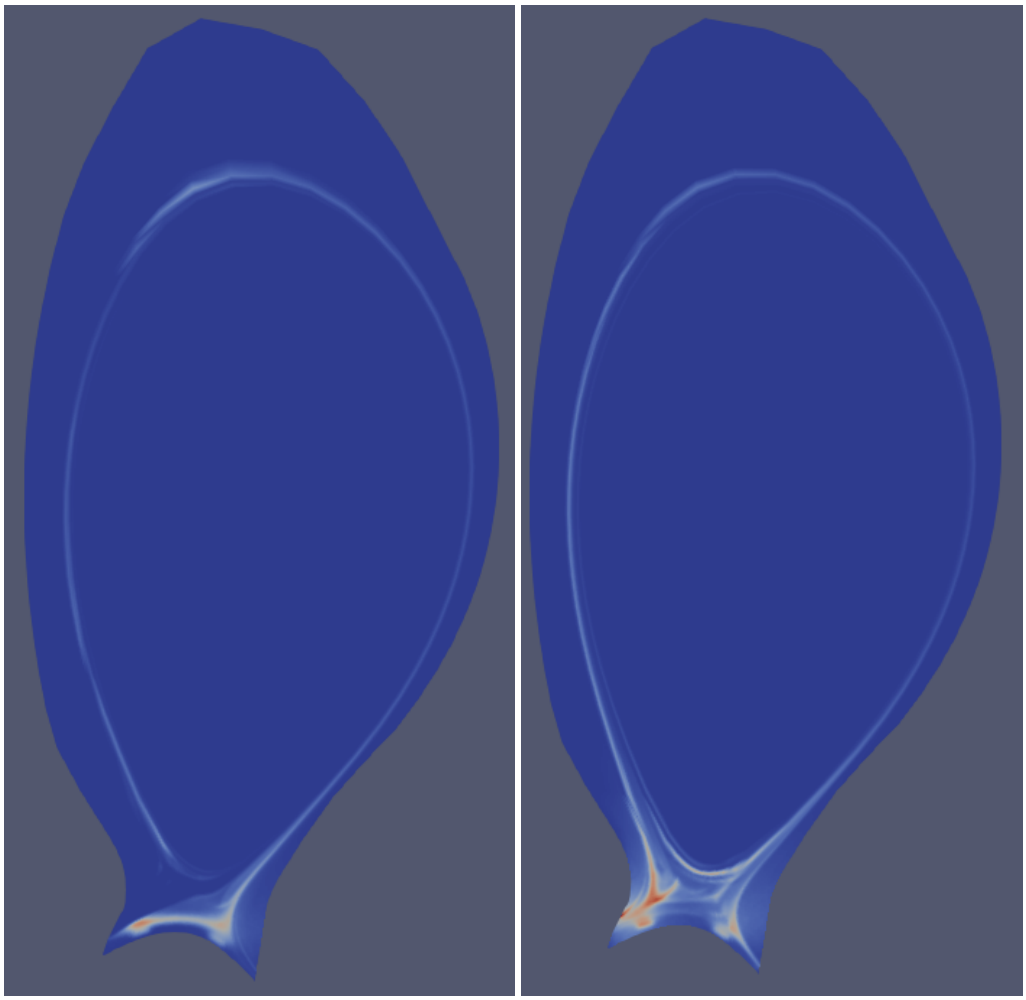

(e) t =14.2 ms

(f) t =15.2 ms

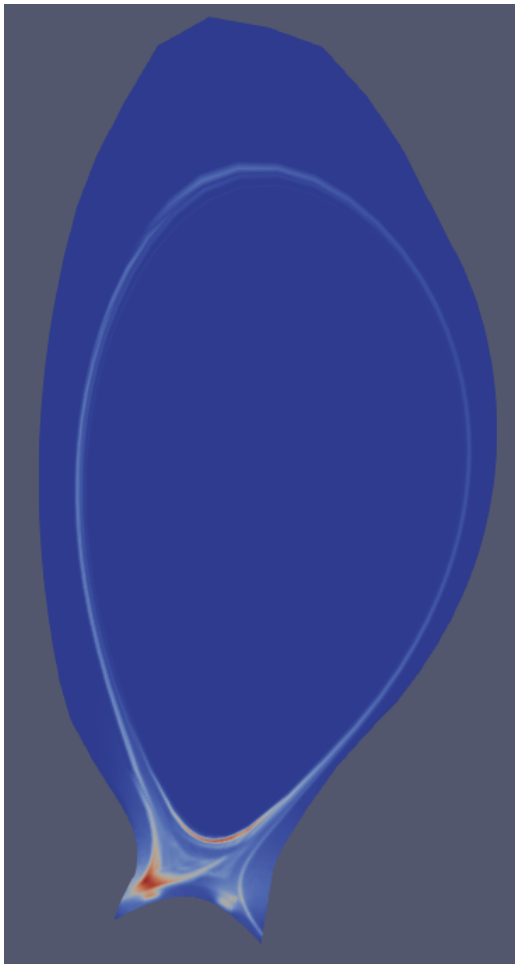

(g) $t = 15.5\,\mathrm{ms}$

Figure 12: Images showing the concentration of nitrogen impurities at different times during the simulation. Initially the nitrogen is mainly concentrated in the private region. Later on it loops around the plasma core twice, resulting in an increase in nitrogen density just above the X-point.

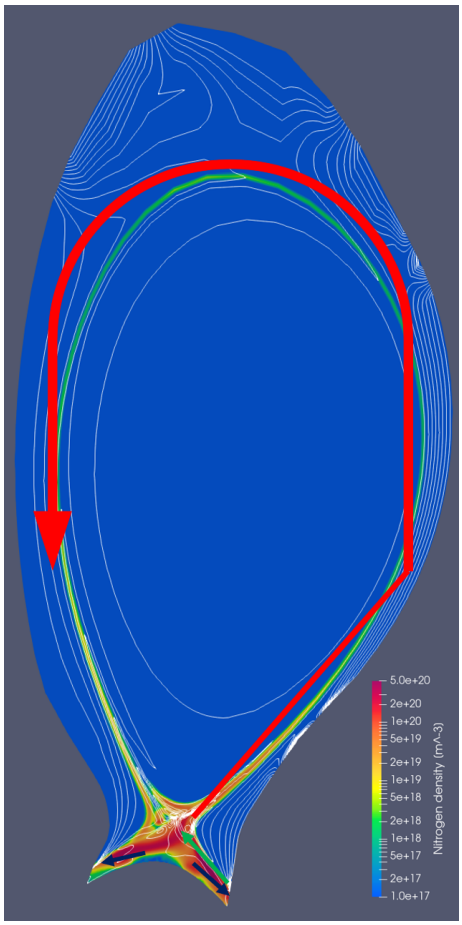

Figure 13: Image showing the contourlines of the electric potential at $t = 13.4\,\mathrm{ms}$, with the nitrogen concentration as the background. The arrows schematically show the distribution of the nitrogen throughout the simulation. First the nitrogen moves along the dark blue arrows towards the strike points. Then the nitrogen pile-up at the outer divertor starts moving towards the X-point, illustrated by the green arrow. After that, two consecutive loops around the core follow, depicted by the red arrow.

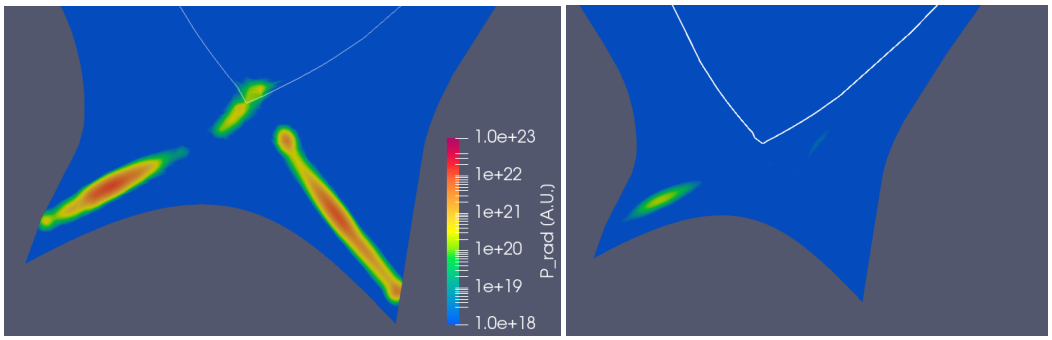

(a) t =13.14 ms (b) t =13.92 ms

(c) t =15.18 ms (d) t =15.49 ms

Figure 14: Images showing the radiation of the nitrogen impurities for different times during the simulation. The white line shows $\psi_N = 1$. Initially the radiation is mainly located along the strike lines, but later on this shifts towards the X-point region, just within the separatrix.

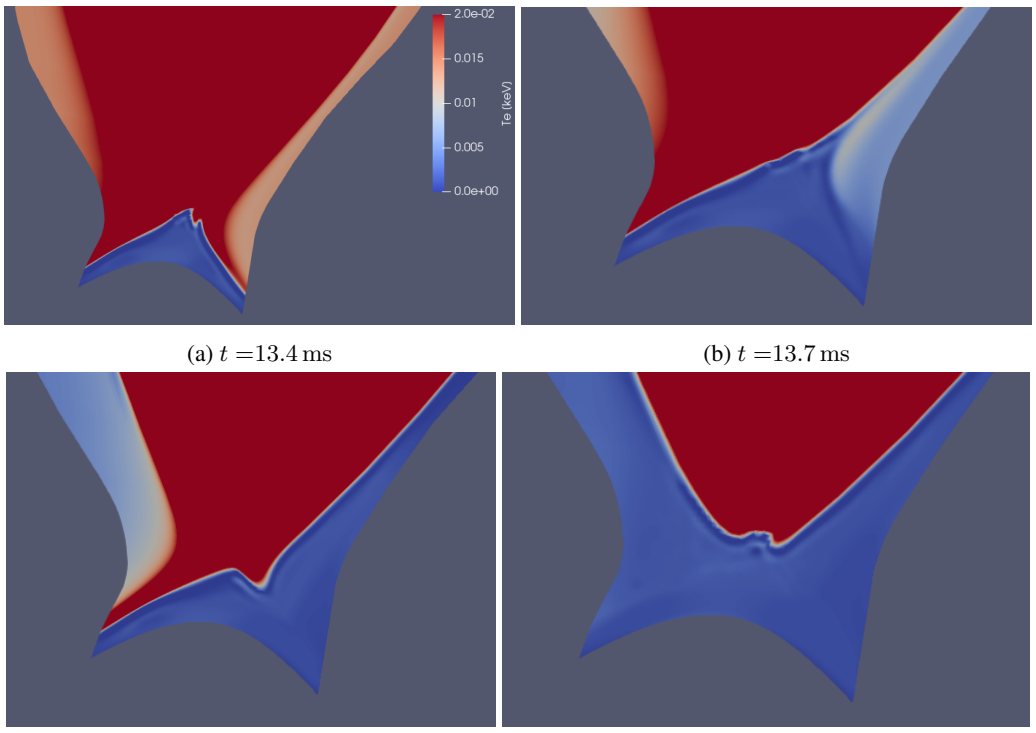

(a) t =13.4 ms (b) t =13.7 ms

(c) t =14.2 ms (d) t =14.9 ms

Figure 15: Images showing the temperature in the private region. Note that the scale is capped at 20 eV, to effectively show where the SOL has cooled down to the single eV range. In these images, it is seen that first the outer leg detaches, then the SOL cools down, and finally the inner leg also detaches.

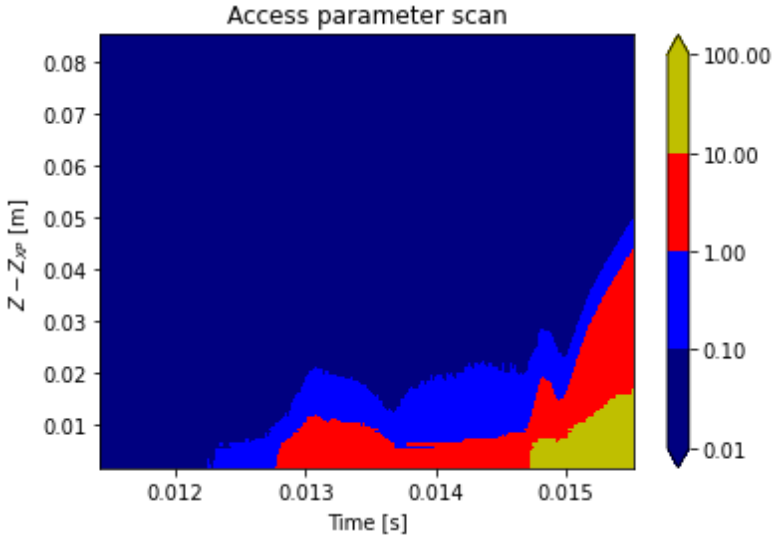

Figure 16: Image showing the value of the XPR access parameter at different locations above the X-point during the simulation. The vertical axis shows the height above the X-point which is located at -0.96 m. An XPR can occur when the access parameter is larger than one, according to [18].

Next, the access parameter is calculated for every tenth time step of the simulation, on a line through the X-point towards the centre of the plasma. Then the value of the parameter is plotted for each time step and location using a contour plot, seen in Figure 16. This plot shows that throughout the simulation for a long time the access parameter is below one at (almost) all locations. Near the end of the simulation more locations close to the X-point reach a value above one.

As can be seen from Figure 16, the access parameter is above one in a region a few centimetres above the X-point during a part of the simulation. It even increases above a value of 10 in the last millisecond. It could be expected that the XPR forms at the location of the highest value of the access parameter. However, when looking Figure 17, the XPR is not as close as possible to the X-point.

This difference can be explained when not only looking at the value of the access parameter. Let's also take into account the nitrogen distribution. As can ben seen in Figure 18a, the density of nitrogen is zero at most times and locations just above the X-point. Near the end of the simulation this changes, with the presence of a banana shaped region of increased nitrogen density, as visible in Figures 12f and 12g. As can be seen from Figure 18a and Figure 18b together, this region of higher nitrogen density is also the region where the radiation is emitted. This is of course as expected, since there can be no nitrogen radiation without nitrogen.

When looking at both Figures 16 and 18 it becomes clear that the access parameter is not the only important factor. At around $t = 13\,\mathrm{ms}$, the value of X_A is above one, and there is a bit of nitrogen located close to the X-point. However, no radiation is observed, and the nitrogen quickly disappears from this area. When higher concentrations of nitrogen are present in an area where the access parameter is above one, radiation starts to rise sharply.

In the model used by Stroth et al. [18], the radiation from impurities is neglected as an access parameter, since initially the temperatures are too high for radiation and impurities will be ionised. However, when the plasma is (partially) cooled down, the presence and radiation from impurities appears to be an important factor in actually forming an XPR.

The simulation does produce an XPR as far as can be verified, since a radiation region just above the X-point is observed. Furthermore, the access parameter at that region is also above one, so an XPR can form there. However, there are some limitations to this modeling, which can be dropped in future work. Even so, these simulations are the first simulations using JOREK that incorporate both deuterium and impurity species. The (ionised) impurities move as expected with the electric potential, showing that the basis of the model works.

During the simulations it became apparent that the puffing rate as well as the ramp time were very important. When these were too high or too short respectively, the simulation would crash before anything

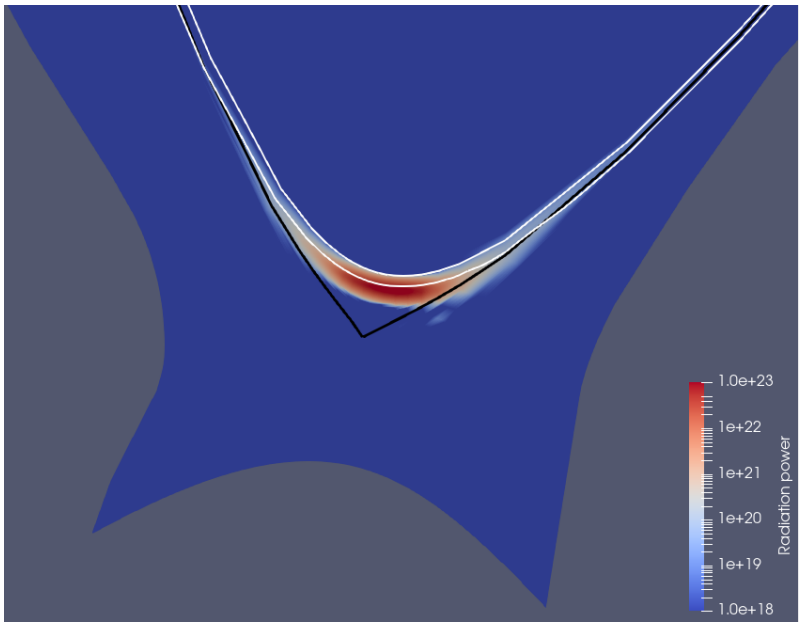

Figure 17: Image showing the radiation of nitrogen at t =15.5 ms in arbitrary units, as well as the contourline for $\psi_N = 1$ in black. This makes it easy to see that the radiation region is located quite a bit above the X-point. Also shown are contourlines for $T = 10$ and $T = 100$ eV in white.

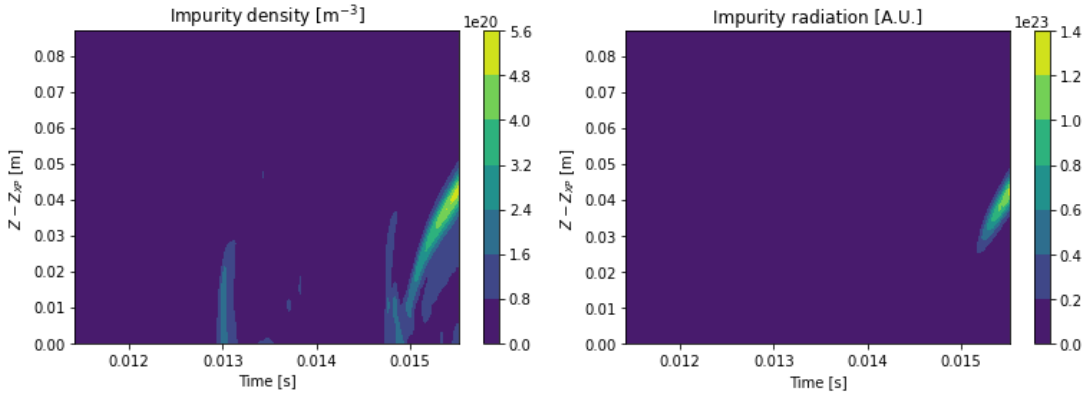

(a) (b)

Figure 18: Graphs showing the (a) impurity density and (b) impurity radiation in a line just above the X-point throughout the simulation.

relevant was observed. It should also be noted that the timescales used in the simulations are a lot shorter than those shown in the paper of Bernert et al. [15]. This is due to the computational cost of running a simulation spanning a longer time. In theory this should not affect the results too much, since these are mainly determined by the amount of nitrogen, but it should not be neglected, since the nitrogen contribution would still keep evolving in the simulation.

Another factor that is not entirely accurate is that the model does not use electrons from the impurities as feedback for the fluid background model. This initial simplification was made assuming that the amount of electrons would be negligible, but this is not justified at high nitrogen concentrations anymore. The nitrogen density reaches $1 \times 10^{20}\,\mathrm{m}^{-3}$ order of magnitude, while the electron density in the fluid background is also of the order of $1 \times 10^{20}\,\mathrm{m}^{-3}$.

An interesting difference between these results and previous modelling is the temperature behaviour when the XPR has formed. SOLPS-ITER modelling showed a higher located XPR, paired with different temperature contour lines, see figure 6 in the work of Stroth et al. [18]. These temperature contours cross more through the plasma than those seen in Figure 17, which stay around $\psi_N = 1$. This could change with a longer simulation, but that is not guaranteed. Future work could explore the reason of these differences, to see if they are due to different solving techniques, or whether it is due to different physics being implemented.

4 Conclusion and Outlook

In this thesis, the physics of XPR formation were studied using the JOREK code with a hybrid fluid-kinetic model. In order to do so, first an axissymmetric reduced MHD simulation with single temperature assumption was started from the equilibrium data obtained from AUG. In this simulation the grid was extended to the true plasma facing components, and the background source and diffusion profiles were set in such a way that the initial density and temperature profiles were approximately constant over time. Then deuterium puffing was added, leading to an increase in electron density in the private region, as well as a progressing “cold-front" upwards towards the X-point over time. This “cold-front" is caused by the ionisation of the neutral deuterium. Next also nitrogen impurities were puffed in the private region. This resulted in detachment of first the outer leg, and then also the inner leg. The nitrogen was transported mainly along the potential contour lines, indicating transport was dominated by the E×B drift. Then also a high radiation zone developed a few centimetres above the X-point, which resembles qualitatively the experimental observations.

The XPR access parameter is an analytical model for the possibility of XPR formation, based on field line stagnation close to the X-point and both neutral and ionised impurity densities. The radiation zone developed in a zone which has been shown to have an access parameter larger than one, which indicates that it can indeed be an XPR. JOREK was able to reproduce these states with an access parameter larger than one, and when combined with sufficient nitrogen, this leads to a localised strong radiation, which resembles expermental observations qualitatively.

The research question for this work was ‘What physics beyond the MHD model are needed to simulate an XPR in AUG?’. To obtain the results, the particle model used charge exchange, ionisation, recombination, and (line) radiation. Also recycling of impurities in neutral form at the plasma-wall interface contributes to the density evolution.

Other questions raised in the introduction were a bit harder to provide factual answers to. During this work no real HFSHD region was seen, so this might support the idea that adding nitrogen suppresses this phenomena. It should be noted that no HFSHD region was seen in deuterium only simulations either, which is probably linked to the long time scales needed for such a formation.

As for the influence of an XPR on pedestal dynamics, a bit more can be said. In the simulations described in this work, the pedastal moved slightly inward. This is visible in Figure 17, which shows the pedestal moving upwards near the X-point.

The simulation that showed the formation of an XPR couldn’t be continued for much longer timescales in the frame of this master thesis project due to the formation of numerical instabilities. No clear cause for this has been found. To investigate this more time and effort would have been needed to repeat simulations with higher grid resolutions, higher marker numbers representing the deuterium neutrals and nitrogen, and possibly smaller timesteps. Another step towards more robust simulations could be to find ‘better’ input parameters. Some options would be a starting equilibrium with less steep gradients, slower ramp-up times for the gas puffing, or lower puff rates in general. The latter two would result in longer runtimes to reach the same quantities of neutral deuterium and nitrogen added to the simulation. Also relevant for the robustness would be to do simulations with stronger parameter variations.

One of the next steps in the simulation of an XPR would be to include the electrons from the nitrogen impurities. As explained in Section 2 the assumption was made that the amount of electrons from the nitrogen is negligible. With (local) nitrogen densities reaching $5 \times 10^{20}\,\mathrm{m}^{-3}$ and electron densities of $1 \times 10^{20}\,\mathrm{m}^{-3}$ this assumption might not be entirely valid anymore. Including the electrons of the impurities when (partly) ionised can add up to seven electrons per nitrogen atom, which can (locally) influence the electron density significantly. Future simulations can be performed to see how such a more accurate treatment of the electron density would influence the XPR formation.

When more robust simulations, preferrably with a better treatment of impurity electrons, have been realised, a next step would be to run 3D simulations. 3D simulations can simulate ELMs, which are not captured in axisymmetric studies. This enables research into the suppression of ELMs by an XPR, as observed in experiments on AUG.

5 References

[1] Garry McCracken and Peter Stott. *Fusion: the energy of the universe*. Academic Press, 2012.

[2] D.J. Griffiths. *Introduction to Electrodynamics*. Cambridge University Press, 4 edition, June 2017.

[3] J.K. Shultis and R.E. Faw. *Fundamentals of Nuclear Science and Engineering*. Taylor & Francis, 2002. ISBN 9780824708344. URL https://books.google.nl/books?id=SO4Lmw8XoEMC.

[4] Jeffrey P Freidberg. *Plasma physics and fusion energy*. Cambridge university press, 2008.

[5] R.A. Dunlap. *An Introduction to the Physics of Nuclei and Particles*. Thomson Brooks/Cole, 2004. ISBN 9780534392949.

[6] Robert Arnoux. How fritz wagner 'discovered' the H-mode. ITER website, June 2009. Accessed on October 20th, 2022, at https://www.iter.org/newsline/86/659.

[7] F. Wagner, G. Becker, K. Behringer, D. Campbell, A. Eberhagen, W. Engelhardt, G. Fussmann, O. Gehre, J. Gernhardt, G. v. Gierke, G. Haas, M. Huang, F. Karger, M. Keilhacker, O. Klüber, M. Kornherr, K. Lackner, G. Lisitano, G. G. Lister, H. M. Mayer, D. Meisel, E. R. Müller, H. Murmann, H. Niedermeyer, W. Poschenrieder, H. Rapp, H. Röhr, F. Schneider, G. Siller, E. Speth, A. Stäbler, K. H. Steuer, G. Venus, O. Vollmer, and Z. Yü. Regime of improved confinement and high beta in neutral-beam-heated divertor discharges of the asdex tokamak. *Phys. Rev. Lett.*, 49:1408–1412, Nov 1982. doi:10.1103/PhysRevLett.49.1408.

[8] P.T. Lang, A. Loarte, G. Saibene, L.R. Baylor, M. Becoulet, M. Cavinato, S. Clement-Lorenzo, E. Daly, T.E. Evans, M.E. Fenstermacher, et al. ELM control strategies and tools: status and potential for ITER. *Nuclear Fusion*, 53(4):043004, 2013.

[9] A. Loarte, G. Saibene, R. Sartori, D. Campbell, M. Becoulet, L. Horton, T. Eich, A. Herrmann, G. Matthews, N. Asakura, A. Chankin, A. Leonard, G. Porter, G. Federici, G. Janeschitz, M. Shimada, and M. Sugihara. Characteristics of type I ELM energy and particle losses in existing devices and their extrapolation to ITER. *Plasma Physics and Controlled Fusion*, 45(9):1549, aug 2003. doi:10.1088/0741-3335/45/9/302.

[10] W.A.J. Vijvers, G.P. Canal, B. Labit, H. Reimerdes, B. Tal, S. Coda, G.C. De Temmerman, B.P. Duval, T.W. Morgan, J.J. Zielinski, and the TCV Team. Power exhaust in the snowflake divertor for l- and h-mode tcv tokamak plasmas. *Nuclear Fusion*, 54(2):023009, feb 2014. doi:10.1088/0029-5515/54/2/023009.

[11] J. Rapp, P. Monier-Garbet, G.F. Matthews, R. Sartori, P. Andrew, P. Dumortier, T. Eich, W. Fundamenski, M. von Hellermann, J. Hogan, L.C. Ingesson, S. Jachmich, H.R. Koslowski, A. Loarte, G. Maddison, D.C. McDonald, A. Messiaen, J. Ongena, V. Parail, V. Philipps, G. Saibene, B. Unterberg, and JET EFDA Contributors. Reduction of divertor heat load in JET ELMy h-modes using impurity seeding techniques. *Nuclear Fusion*, 44(2):312, jan 2004. doi:10.1088/0029-5515/44/2/013.

[12] S. I. Krasheninnikov, A. S. Kukushkin, and A. A. Pshenov. Divertor plasma detachment. *Physics of Plasmas*, 23(5):055602, 2016. doi:10.1063/1.4948273.

[13] S.I. Krasheninnikov and A.S. Kukushkin. Physics of ultimate detachment of a tokamak divertor plasma. *Journal of Plasma Physics*, 83(5), 2017.

[14] A. W. Leonard. Plasma detachment in divertor tokamaks. *Plasma Physics and Controlled Fusion*, 60 (4):044001, feb 2018. doi:10.1088/1361-6587/aaa7a9.

[15] M. Bernert, F. Janky, B. Sieglin, A. Kallenbach, B. Lipschultz, F. Reimold, M. Wischmeier, M. Cavedon, P. David, M.G. Dunne, M. Griener, O. Kudlacek, R.M. McDermott, W. Treutterer, E. Wolfrum, D. Brida, O. Février, S. Henderson, and M. Komm. X-point radiation, its control and an ELM suppressed radiating regime at the ASDEX upgrade tokamak. *Nuclear Fusion*, 61(2):024001, dec 2020. doi:10.1088/1741-4326/abc936.

[16] S. Potzel, M. Wischmeier, M. Bernert, R. Dux, F. Reimold, A. Scarabosio, S. Brezinsek, M. Clever, A. Huber, A. Meigs, and M. Stamp. Formation of the high density front in the inner far sol at asdex upgrade and jet. *Journal of Nuclear Materials*, 463:541–545, 2015. ISSN 0022-3115. doi:https://doi.org/10.1016/j.jnucmat.2014.12.008. PLASMA-SURFACE INTERACTIONS 21.

[17] M. G. Dunne, S. Potzel, F. Reimold, M. Wischmeier, E. Wolfrum, L. Frassinetti, M. Beurskens, P. Bilkova, M. Cavedon, R. Fischer, B. Kurzan, F. M. Laggner, R. M. McDermott, G. Tardini, E. Trier, E. Viezzer, M. Willensdorfer, The EUROfusion MST1 Team, and The ASDEX-Upgrade Team. The role of the density profile in the asdex-upgrade pedestal structure. *Plasma Physics and Controlled Fusion*, 59(1):014017, oct 2016. doi:10.1088/0741-3335/59/1/014017.

[18] U Stroth, M Bernert, D Brida, M Cavedon, R Dux, E Huett, T Lunt, O Pan, M Wischmeier, the ASDEX Upgrade Team, et al. Model for access and stability of the x-point radiator and the threshold for marfes in tokamak plasmas. *Nuclear Fusion*, 62(7):076008, 2022.

[19] S. Wiesen, D. Reiter, V. Kotov, M. Baelmans, W. Dekeyser, A.S. Kukushkin, S.W. Lisgo, R.A. Pitts, V. Rozhansky, G. Saibene, I. Veselova, and S. Voskoboynikov. The new solps-iter code package. *Journal of Nuclear Materials*, 463:480–484, 2015. ISSN 0022-3115. doi:https://doi.org/10.1016/j.jnucmat.2014.10.012. PLASMA-SURFACE INTERACTIONS 21.

[20] M. Hoelzl, G.T.A. Huijsmans, S.J.P. Pamela, M. Bécoulet, E. Nardon, F.J. Artola, B. Nkonga, C.V. Atanasiu, V. Bandaru, A. Bhole, D. Bonfiglio, A. Cathey, O. Czarny, A. Dvornova, T. Fehér, A. Fil, E. Franck, S. Futatani, M. Gruca, H. Guillard, J.W. Haverkort, I. Holod, D. Hu, S.K. Kim, S.Q. Korving, L. Kos, I. Krebs, L. Kripner, G. Latu, F. Liu, P. Merkel, D. Meshcheriakov, V. Mitterauer, S. Mochalskyy, J.A. Morales, R. Nies, N. Nikulsin, F. Orain, J. Pratt, R. Ramasamy, P. Ramet, C. Reux, K. Särkimäki, N. Schwarz, P. Singh Verma, S.F. Smith, C. Sommariva, E. Strumberger, D.C. van Vugt, M. Verbeek, E. Westerhof, F. Wieschollek, and J. Zielinski. The JOREK non-linear extended mhd code and applications to large-scale instabilities and their control in magnetically confined fusion plasmas. *Nuclear Fusion*, 61(6):065001, may 2021. doi:10.1088/1741-4326/abf99f.

[21] SQ Korving, GTA Huijsmans, J-S Park, A Loarte, JOREK Team, et al. Development of the neutral model in the nonlinear MHD code JOREK: Application to E× B drifts in ITER PFPO-1 plasmas. *Physics of Plasmas*, 30(4), 2023.

[22] R Betti and OA Hurricane. Inertial-confinement fusion with lasers. *Nature Physics*, 12(5):435–448, 2016.

[23] Sam Taylor. *Photoionisation and Spacecraft-Shadow Interactions in Saturn's Inner Magnetosphere*. PhD thesis, 08 2019.

[24] Niek Lopez Cardozo. Lecture notes: fusion on the back of an envelope. Internal website, TU/e, 2019.

[25] Nathaniel J. Fisch. Theory of current drive in plasmas. *Rev. Mod. Phys.*, 59:175–234, Jan 1987. doi:10.1103/RevModPhys.59.175.

[26] LA Artsimovich. Tokamak devices. *Nuclear Fusion*, 12(2):215, 1972.

[27] Francesco Romanelli. Fusion energy. *EPJ Web of Conferences*, 246:00013, 01 2020. doi:10.1051/epjconf/202024600013.

[28] A. A. Ware. Pinch effect for trapped particles in a tokamak. *Phys. Rev. Lett.*, 25:15–17, Jul 1970. doi:10.1103/PhysRevLett.25.15.

[29] Timo Ravensbergen, Matthijs van Berkel, Artur Perek, C Galperti, BP Duval, O Février, RJR van Kampen, F Felici, JT Lammers, Christian Theiler, et al. Real-time feedback control of the impurity emission front in tokamak divertor plasmas. *Nature communications*, 12(1):1105, 2021.

[30] Debojyoti Ghosh, Mikhail Dorf, Milo Dorr, and Jeffrey Hittinger. Kinetic simulation of collisional magnetized plasmas with semi-implicit time integration. *Journal of Scientific Computing*, 77, 11 2018. doi:10.1007/s10915-018-0726-6.

[31] GF Matthews. Plasma detachment from divertor targets and limiters. *Journal of nuclear materials*, 220:104–116, 1995.

[32] K. Strien. A particle model for impurities in magnetohydrodynamics simulations of shattered pellet injection. Master's thesis, Eindhoven University of Technology, June 2022.

[33] A. W. Leonard. Edge-localized-modes in tokamaks. *Physics of Plasmas*, 21(9):090501, 09 2014. ISSN 1070-664X. doi:10.1063/1.4894742.

[34] Robert G. Kleva and Parvez N. Guzdar. Fast disruptions by ballooning mode ridges and fingers in high temperature, low resistivity toroidal plasmas. *Physics of Plasmas*, 8(1):103–109, 01 2001. ISSN 1070-664X. doi:10.1063/1.1331098.

[35] P. B. Snyder, H. R. Wilson, J. R. Ferron, L. L. Lao, A. W. Leonard, T. H. Osborne, A. D. Turnbull, D. Mossessian, M. Murakami, and X. Q. Xu. Edge localized modes and the pedestal: A model based on coupled peeling–ballooning modes. *Physics of Plasmas*, 9(5):2037–2043, 04 2002. ISSN 1070-664X. doi:10.1063/1.1449463.

[36] J Ongena, R Koch, R Wolf, and H Zohm. Magnetic-confinement fusion. *Nature Physics*, 12(5): 398–410, 2016.

[37] A Cathey, M Hoelzl, G Harrer, M G Dunne, G T A Huijsmans, K Lackner, S J P Pamela, E Wolfrum, S Günter, the JOREK Team, the ASDEX Upgrade Team, and the EUROfusion MST1 Team. MHD simulations of small ELMs at low triangularity in ASDEX upgrade. *Plasma Physics and Controlled Fusion*, 64(5):054011, apr 2022. doi:10.1088/1361-6587/ac5b4b.

[38] GTA Huysmans. External kink (peeling) modes in x-point geometry. *Plasma physics and controlled fusion*, 47(12):2107, 2005.

[39] Olivier Czarny and Guido Huysmans. Bézier surfaces and finite elements for mhd simulations. *Journal of Computational Physics*, 227(16):7423–7445, 2008. ISSN 0021-9991. doi:https://doi.org/10.1016/j.jcp.2008.04.001.

[40] JOREK team. JOREK website, 2022. https://www.jorek.eu/.

[41] Hong Qin, Shuangxi Zhang, Jianyuan Xiao, Jian Liu, Yajuan Sun, and William M. Tang. Why is Boris algorithm so good? *Physics of Plasmas*, 20(8):084503, 08 2013. ISSN 1070-664X. doi:10.1063/1.4818428.

[42] Daniël Cornelis van Vugt. Nonlinear coupled mhd-kinetic particle simulations of heavy impurities in tokamak plasmas. 2019.